

Simultaneous positioning and orientation of a single nano-object by flow control: theory and simulations

Pramod P Mathai^{1,2,4,5}, Andrew J Berglund¹,
J Alexander Liddle¹ and Benjamin A Shapiro³

¹ Center for Nanoscale Science and Technology (CNST) at the National Institute of Standards and Technology (NIST), Gaithersburg, MD 20899, USA

² Institute for Research in Electronics and Applied Physics, University of Maryland (UMD), College Park, MD 20742, USA

³ Department of Bioengineering, UMD, College Park, MD 20742, USA
E-mail: pramod.mathai@nist.gov

New Journal of Physics **13** (2011) 013027 (27pp)


Received 12 April 2010

Published 19 January 2011

Online at <http://www.njp.org/>

doi:10.1088/1367-2630/13/1/013027

Abstract. In this paper, we theoretically describe a method to simultaneously control both the position and orientation of single nano-objects in fluids by precisely controlling the flow around them. We develop and simulate a control law that uses electro-osmotic flow (EOF) actuation to translate and rotate rigid nano-objects in two spatial dimensions. Using EOF to control nano-objects offers advantages as compared to other approaches: a wide class of objects can be manipulated (no magnetic or electric dipole moments are needed), the object can be controlled over a long range ($>100\ \mu\text{m}$) with sub-micrometer accuracy, and control may be achieved with simple polydimethylsiloxane (PDMS) devices. We demonstrate the theory and numerical solutions that will enable deterministic control of the position and orientation of a nano-object in solution, which can be used, for example, to integrate nanostructures in circuits and orient sensors to probe living cells.

 Online supplementary data available from stacks.iop.org/NJP/13/013027/mmedia

⁴ Author to whom any correspondence should be addressed.

⁵ PPM is in joint appointment with CNST, NIST, Gaithersburg, MD, USA and Institute of Research in Electronics and Applied Physics, UMD, College Park, USA.

Contents

1. Introduction	2
2. Electro-osmotic flow	4
3. Translational and rotational velocity of an ellipsoid in electro-osmotic flow (EOF)	5
3.1. Translational and rotational Brownian motion of an ellipsoid	9
4. Feedback control of the object's position and orientation	9
4.1. Non-dimensionalized equations for the feedback loop	12
5. Numerical simulations of an ellipsoid's manipulation	14
5.1. The Fokker–Planck equation describing the orientation error	18
6. Additional considerations towards experiments	23
7. Conclusion	24
Acknowledgments	25
References	25

1. Introduction

We theoretically describe a technique for simultaneously positioning and orienting single nano-objects in a fluid in two spatial dimensions by manipulating the flow around them. We address two object control goals with this technique. The first is the ability to move the object across large distances (tens of micrometers). The second is the ability to accurately control the position and orientation of objects of a variety of shapes and material properties—for example, semiconductors [1], conductors [2] and dielectrics [3].

Previously, we showed simulations demonstrating *position* control of *spherical* objects [4] in a microfluidic device using electro-osmotic flow (EOF) control. The ideas developed in that study enabled an experimental demonstration of position control of micrometer-sized spherical objects to sub-micrometer accuracy [5] and subsequently the control of nanoscopic particles (single quantum dots) to nanometer precision [6]. In this paper, we explain and simulate a technique that shows how the translational and *shear* components of the flow field in the device can be manipulated, to trap an object at a desired position and orientation or manipulate both its position and orientation along a desired trajectory.

Existing approaches for simultaneously controlling the position and orientation of a single (or a few) object(s) can be classified into actuation strategies that include optical, magnetic and electrical techniques. If objects have a higher refractive index than their surrounding medium, a laser beam can be used to attract the object into the region of highest light intensity. Variations of this basic principle have been used to transfer translational and angular momentum from the laser beam to the object either by making use of special optical properties of the object or by manipulating the wave front of the incident light [7]–[13].

Magnetic fields in combination with fluidic forces have been used to control magnetic objects [14] or with a combination of optical forcing for translation and electromagnets for rotation [15]. Apart from the requirement that the object be magnetic, the objects may require specially designed shapes to enable fluidic actuation [16]. Alternatively, magnetic features are lithographically patterned on objects to allow manipulation of their orientation by magnetic fields [17].

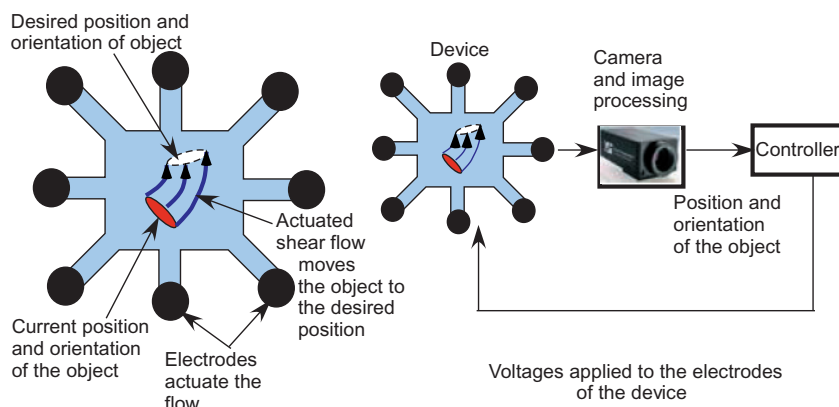


Figure 1. The left panel shows a schematic diagram of the top view of the proposed device. The electrodes actuate a flow that translates and rotates the object from its current to its desired position and orientation. The right panel shows the feedback loop that achieves flow control in the device. At every instant, a camera captures an image of the object and an image processing algorithm computes the position and orientation of the object and transmits that information to the controller. The controller uses this information to actuate a flow in the device (by creating an electric field that moves the fluid in the device) that translates and rotates the object to the desired position and orientation.

If the object has a significant dipole moment, dielectrophoresis (a type of electric actuation) can be used to position and orient nanowires [18]–[23] and biological cells [24]. In this technique, a high electric field gradient interacts with the object’s dipole moment to translate and rotate the object. Since the electric field gradients have to be high, the object is controlled near an electrode in a device where the gradient is steep.

The position and orientation control that we present below uses electrical actuation to modulate the flow around an object. Our technique depends on controlling viscous drag, a force that applies to every object, and can hence be used to control a general class of object—the object does not have to be charged or magnetic or have any other special properties. Our simulations will show that the object can be controlled across a large ($\approx 100 \mu\text{m}$) region. The approach uses feedback control of shear flow in a microfluidic device to translate and rotate the object. The fluidic shear force acting on the object (which is assumed to be inertia-less) suspended in the fluid rotates the object to any desired orientation (left panel of figure 1), while the translational component of the fluidic drag moves it to any desired location in a two-dimensional (2D) control region. The position and orientation of the object, which are randomly perturbed due to Brownian motion, are measured at regular intervals. From this visual measurement, a feedback control loop determines and applies the fluid flow that will translate and rotate the object from where it is towards where it should be (see right panel of figure 1).

The flow is actuated electro-osmotically. Here, the electric field moves the fluid, which moves the object by viscous forces [25, 26] (which is different from electrophoretic or dielectrophoretic actuation where the electric field creates a force directly on a charged or polarizable object). By using multiple (here eight) electrodes in concert (see figure 2), it is possible to create complex electric field patterns in space, and in our thin planar devices those patterns are faithfully transmitted to the fluid flow in the control region. Feedback control of

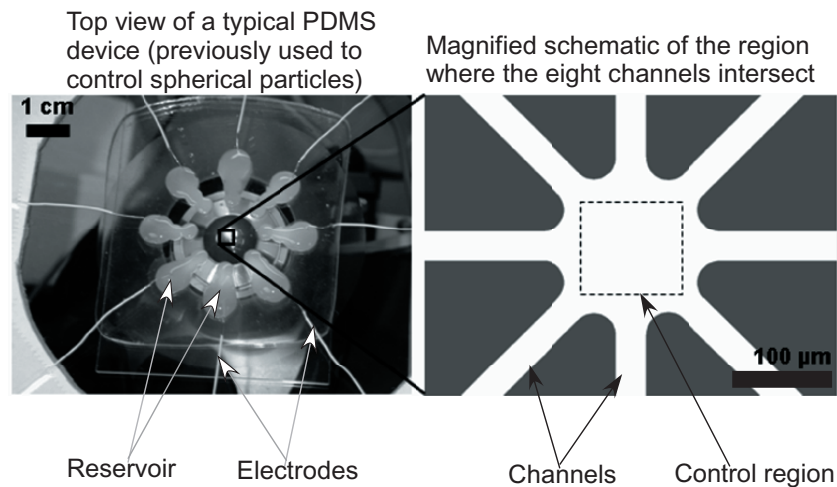


Figure 2. The left panel shows the top view of a typical flow control device. The device is made of polydimethylsiloxane (PDMS) and consists of eight channels that merge into a central region. The electrodes are immersed in reservoirs connected to the channels. The fluid and objects are injected into the reservoirs and then flow into the central region where the channels merge. A magnified schematic diagram of this central region is shown in the right panel. The square region (shown with a dotted black line in the right panel) is the $100\ \mu\text{m} \times 100\ \mu\text{m}$ control region.

those patterns in time has allowed us to control the position of single objects [6] and is here being extended to also allow control of their orientation.

The rest of the paper is organized as follows. Section 2 describes electro-osmotic flow. Section 3 describes the effect of the fluid on the motion of the object. Section 4 discusses the control algorithm that is used to manipulate the flow around the object. We show numerical examples demonstrating object control in section 5 and end with a discussion of additional considerations towards experiments in sections 6 and 7.

2. Electro-osmotic flow

At the interface between solid and an electrolytic fluid, the surface energy of the solid surface is reduced by the adsorption of ions from the fluid onto the oppositely charged ions at the surface of the solid [25, 26]. This results in a charge imbalance in a thin ($<100\ \text{nm}$) fluid layer, termed the diffuse (or Debye) layer, adjacent to the wall–fluid interface of the device.

A potential difference applied at the electrodes creates a planar electric field $\vec{E}(\hat{x}, \hat{y})$ in the plane of the device. That electric field moves the ions in the Debye layer, which in turn drags the rest of the fluid in the device due to viscosity. The flow is laminar (Reynolds number $Re < 10^{-4}$), has a steady-state velocity profile $\vec{U}(\hat{x}, \hat{y})$ of a plug flow (that is constant along \hat{z} apart from the variation in the thin Debye layer as shown in figure 3) that is linearly proportional to the applied electric field and has the value [25]

$$\vec{U}(\hat{x}, \hat{y}) = \frac{\epsilon\zeta}{\mu} \cdot \vec{E}(\hat{x}, \hat{y}), \quad (1)$$

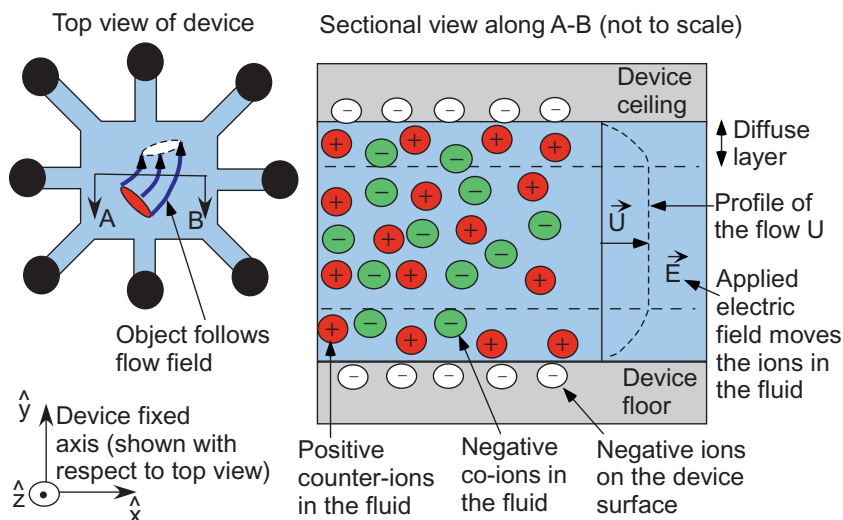


Figure 3. Flow profile in the device (the figure in the right panel is modified from [25]): The negatively charged surface of the device is shielded by positively charged ions from the electrolyte solution. The ions in the thin diffuse (Debye) layer near the device–fluid interface move under the influence of the electric field and drag the rest of the fluid by viscous forces [25]. The resulting flow profile is uniform along \hat{z} (except for the variation in the thin diffuse layer, not drawn to scale in the figure) with the flow velocity \vec{U} proportional to the applied electric field \vec{E} .

where μ and ϵ are the dynamic viscosity and permittivity of the fluid, respectively, and ζ is the potential difference across \hat{z} between the edge of the Debye layer and the device–fluid interface.

Since the electric field is irrotational (curl-free) the fluid velocity in the device, which follows the local electric field, is also irrotational. This means that EOF can only impart a translational velocity to a spherical object—one cannot rotate a sphere using EOF. However, as described in the next section, EOF can translate as well as rotate a non-spherical object such as an ellipsoid or a nanorod.

3. Translational and rotational velocity of an ellipsoid in electro-osmotic flow (EOF)

Similar to the inertia-free spherical particles⁶ used previously to demonstrate positional control [4, 5], an inertia-free ellipsoid will instantaneously translate along the stream lines of any flow that is set up in the device. If the flow in the device was rotational, one could create a vortex flow and the rotational velocity of a spherical object would be proportional to the vorticity

⁶ A simple calculation using Newton’s laws [4] shows that a spherical particle of diameter $10\ \mu\text{m}$ with a density equal to that of water takes $0.04\ \text{ms}$ to reach the ambient translational flow velocity. This interval is small compared to the expected $10\ \text{ms}$ between successive control updates, which allows us to assume that the nanorods (major axis length of $10\ \mu\text{m}$ and minor axis length of $200\ \text{nm}$) have negligible inertia and their velocity instantaneously conforms to the local flow field. If the moment of inertia of the sphere is denoted as I_s and the rotational drag coefficient as Ω_s , then a similar calculation for rotation shows that a time $t_r = \frac{I_s \cdot \log(\beta)}{\Omega_s} = \frac{\rho a^2 \log(\beta)}{15\mu}$ is needed for the sphere to reach within $\frac{1}{\beta}$ of the ambient rotational flow velocity of the fluid (ρ and μ are the density and viscosity of the fluid, respectively, and a is the sphere radius). For the above sphere in water, $t_r \approx 0.01\ \text{ms}$ for $\beta = 1000$.

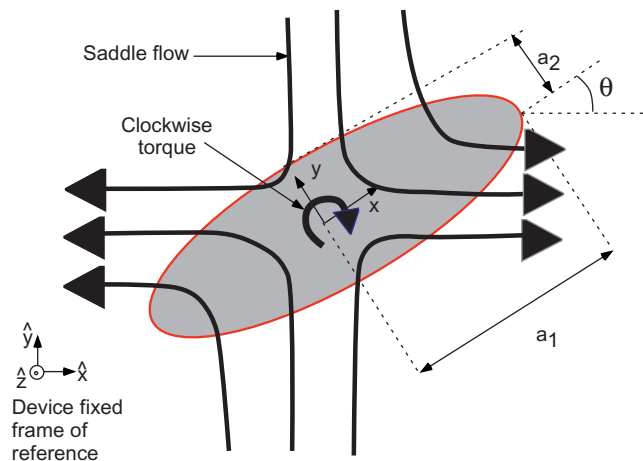


Figure 4. The total torque acting on the body is the sum of infinitesimal torques due to the shear force acting throughout the boundary of the ellipsoid. Due to the unequal axes lengths of the ellipsoid, a saddle flow (illustrated above) can be shown to rotate the ellipsoid clockwise [29]. The body-fixed frame of reference is x – y , and the device-fixed frame is \hat{x} – \hat{y} .

of the flow. However, for an *irrotational* flow, one can nevertheless rotate an ellipsoid due to the interaction of the individual shear components of the flow and the reduced symmetry of the ellipsoid (as compared to a sphere) as shown below. After computing the flow velocity, exact expressions for the force and torque acting on an ellipsoid [29] can be obtained by summing the infinitesimal shear force components (and the resultant torques) acting on every point of the ellipsoid's boundary. For the saddle flow shown in figure 4, the net fluidic torque will rotate the ellipsoid clockwise.

The slow, viscous, incompressible and isothermal flow that is electro-osmotically set up in the device is well described by Stokes flow [29], which neglects the momentum of the fluid in the Navier–Stokes equations of fluid dynamics. The ellipsoid is controlled in a plane parallel to the floor of the device and is assumed to lie far enough (>200 nm) from the floor and ceiling of the device to neglect increased drag due to wall effects [30]. This claim is supported by recent calculations [31], which can be applied, for example, to compute the drag correction terms for a cylindrical particle of diameter 200 nm and length $2\ \mu\text{m}$, with the nearest point on its surface located at a distance $d = 200$ nm from a plane wall, and its axis tilted at an angle ϕ to the plane of the wall. Detailed simulations [31], performed for such cylinders (with aspect ratios of 10), show that the correction term for the (x, y) translational drag coefficients and the rotational drag coefficient about the z -axis are each less than 15% as compared to the unbounded fluid drag coefficients for ϕ as large as 45° . The correction terms decrease as the aspect ratio of the cylinder increases because a proportionately lower area of the rod is close to the wall [31]. Hence, we disregard the wall-correction term and use the unbounded fluid drag coefficients in what follows.

The flow setup in the device is perturbed by the presence of the ellipsoid [32]–[34]. The linear nature of Stokes flow can be exploited to obtain the force and torque acting on *any* body (not just an ellipsoid) that is immersed and free to move in the flow. Denote the surface of the ellipsoid by $\frac{x^2}{a_1^2} + \frac{y^2}{a_2^2} + \frac{z^2}{a_3^2} = 1$ (here we consider ellipsoids where $a_3 = a_2$ and $a_1 > a_2$, so a_1 is the

semi-major axis length and a_2 is the semi-minor axis length of the ellipsoid). The unperturbed flow field $\vec{u}(\vec{r})$ (i.e. the flow that would be observed if no object were present) in the device is approximated to be a superposition of uniform and pure-shear flow fields, i.e. spatial variations of $\vec{u}(\vec{r})$ of $O(a_1^2)$ or higher are neglected.

Denote the translational velocity of the ellipsoid along the device-fixed axes \hat{x} , \hat{y} (see figure 4) by $U_{\hat{x}}$ and $U_{\hat{y}}$, respectively. As shown in figure 4, θ is the angle between the body and device fixed frames of reference. Denote the angular velocity of the ellipsoid about the \hat{z} -axis by ω_z . Denote by \hat{u} and \hat{v} the components of the unperturbed uniform flow along the \hat{x} - and \hat{y} -axes, respectively, evaluated at the position that is occupied by the center of the ellipsoid, while the terms $\frac{\partial \hat{u}}{\partial \hat{x}}$, $\frac{\partial \hat{u}}{\partial \hat{y}}$, $\frac{\partial \hat{v}}{\partial \hat{x}}$ and $\frac{\partial \hat{v}}{\partial \hat{y}}$ represent the shear components of the flow. The constant $e = \frac{a_2}{a_1}$ is the ratio of the minor to major axis lengths of the ellipsoid. For the flow $\vec{u}(\vec{r})$ described above, ignoring parasitic pressure flows and using the assumption of negligible inertia of the ellipsoid, it can be shown [29] that the translational velocity of the ellipsoid matches the uniform flow field component

$$\begin{aligned} U_{\hat{x}} &= \hat{u}, \\ U_{\hat{y}} &= \hat{v} \end{aligned} \quad (2)$$

and the rotational velocity of the ellipsoid is given by

$$\begin{aligned} \omega_z &= \frac{1}{2} \left[\left(\frac{\partial \hat{v}}{\partial \hat{x}} - \frac{\partial \hat{u}}{\partial \hat{y}} \right) + \frac{1-e^2}{1+e^2} \left(\frac{\partial \hat{u}}{\partial \hat{x}} (-\sin(2\theta)) + \frac{\partial \hat{v}}{\partial \hat{x}} (\cos(2\theta)) \dots \right. \right. \\ &\quad \left. \left. + \frac{\partial \hat{u}}{\partial \hat{y}} (\cos(2\theta)) + \frac{\partial \hat{v}}{\partial \hat{y}} (\sin(2\theta)) \right) \right]. \end{aligned} \quad (3)$$

Equations (2) and (3) are derived by integrating the shear and pressure distributions on the surface of the inertia-less ellipsoid after solving the quasi-static Stokes equations [27] (see section A of the supplementary information for more details, available from stacks.iop.org/NJP/13/013027/mmedia). Even if higher order spatial flow variations were considered (in addition to uniform and pure shear flow terms), successive correction terms in equations (2) and (3) would differ by the operator $D^2 \equiv a_i^2 \frac{\partial^2}{\partial x_i^2}$, where x_i are the axis coordinates [34]. In the proposed device, these higher-order terms are of the order $O(a_i^2/r_{\text{dev}}^2)$ and higher compared to the linear terms included in equations (2) and (3); here r_{dev} is the distance from the center of the control region to the midpoint of any straight edge at the boundary in figure 5. Since $\frac{a_1}{r_{\text{dev}}}$ is 0.1 or smaller in the proposed device, we ignore higher spatial order flow variations.

Equation (3) can be simplified by making use of two relations between the four shear components. By continuity, the divergence of the flow field is zero, i.e. $\frac{\partial \hat{u}}{\partial \hat{x}} + \frac{\partial \hat{v}}{\partial \hat{y}} = 0$. We also have that in EOF, since the fluid velocity is proportional to the electric field (as explained in the previous section), the flow field is curl-free—i.e. the component of the the vorticity about the \hat{z} -axis $(\frac{\partial \hat{v}}{\partial \hat{x}} - \frac{\partial \hat{u}}{\partial \hat{y}})$ (the first term of equation (3)) is identically zero. This simplifies equation (3) to

$$\omega_z = \frac{1-e^2}{1+e^2} \left[\frac{\partial \hat{u}}{\partial \hat{y}} (\cos(2\theta)) + \frac{\partial \hat{v}}{\partial \hat{y}} (\sin(2\theta)) \right]. \quad (4)$$

Thus, if we apply an electric field that creates the unperturbed flow field (\hat{u}, \hat{v}) in the device, then this flow will instantaneously turn the ellipsoid with the rotational velocity ω_z in equation (4).

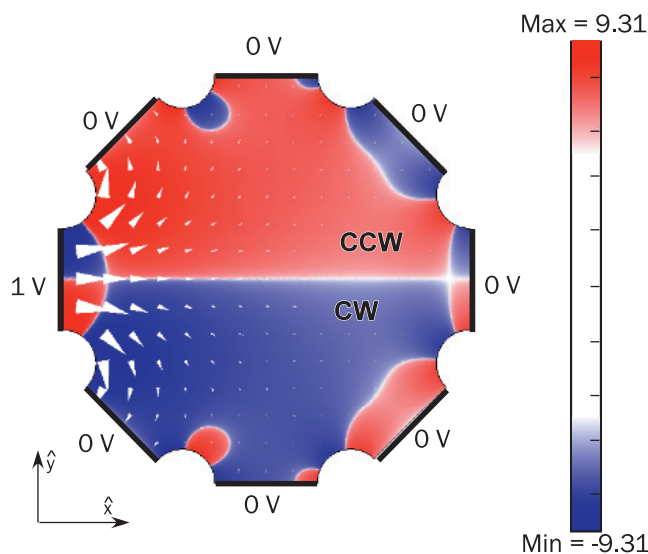


Figure 5. Pre-computed steady-state electric field in the region where the channels intersect (using COMSOL, www.comsol.com⁷). The leftmost edge is maintained at 1 V and all the others are maintained at 0 V. The electric field $E(\hat{x}, \hat{y})$ (which is responsible for the object’s translation) is shown with white arrowheads. The color plot shows the ellipse rotation that will be created. For an ellipsoid oriented at $\theta = 0^\circ$, the shear component $\frac{\partial}{\partial \hat{y}}(E_{\hat{x}}(\hat{x}, \hat{y}))$ decides the direction of the ellipsoid’s rotation (see equation (4)). Thus, in the reddish hued region, the ellipsoid will turn counterclockwise (seeing into the paper), and in the bluish hued region it will turn clockwise. We plot $\text{sign}(\frac{\partial}{\partial \hat{y}}(E_{\hat{x}}(\hat{x}, \hat{y}))) \log_{10}(|\frac{\partial}{\partial \hat{y}}(E_{\hat{x}}(\hat{x}, \hat{y}))|)$ to show both the sign and magnitude of the rotation creating term, which varies between $\approx \pm 10^9 \text{ V m}^{-2}$.

Since the flow velocity components \hat{u} and \hat{v} are linearly dependent on the electric field, the translational and rotational velocities of the object are also linearly dependent on the electric field—a fact that is used in the control algorithm. For any arbitrary orthotropic object (an object with three mutually perpendicular planes of symmetry) like the ellipsoidal rod (or other bodies like right elliptical cylinders and rectangular parallelepipeds), the exact same analysis that has been used in this section can be applied to obtain the translational and rotational velocities; the only difference will be a different shape-dependent constant, instead of $\frac{1-e^2}{1+e^2}$, in equation (4) [28]. For non-orthotropic objects there will be an additional dependence of the rotational velocity of the object on the fluid velocity (and not just the fluid shear as in equation (4)). This is because the force at a particular point on the boundary of the body can give rise to a torque that is not balanced by an opposing torque (due to a lack of sufficient symmetry in the body), thus causing the body to rotate [29]. There will also be an additional dependence of the translational velocity of the object on the fluid shear (and not just the fluid velocity as in equation (2)). As explained later, this kind of coupling between the translational and rotational motions of the object can be included by experimenting with an appropriate gain parameter in the control algorithm.

⁷ All references to commercial products in this paper are provided only to document how results have been obtained. Their identification does not imply recommendation or endorsement by NIST.

3.1. Translational and rotational Brownian motion of an ellipsoid

Thermal equilibrium between the fluid and any object suspended in it is maintained by the random collisions between the object and the surrounding fluid molecules. The object translates and rotates in a time interval dt along random directions by an amount that is, on average, proportional to \sqrt{dt} . Expressions for the translational and rotational diffusion coefficients [35] of an ellipsoid are given in section B of the supplementary information (available from stacks.iop.org/NJP/13/013027/mmedia). For the ellipsoids in our simulation (semi-major axis length $a_1 = 5 \mu\text{m}$ and semi-minor axis length $a_2 = a_3 = 100 \text{ nm}$) that are immersed in water of viscosity (8.9×10^{-4}) Pa s at 300 K, the translational diffusion coefficient along the major axis is $0.306 \mu\text{m}^2 \text{ s}^{-1}$ and along the minor axis is $0.199 \mu\text{m}^2 \text{ s}^{-1}$. The rotational diffusion coefficient about \hat{z} is $0.0197 \text{ rad}^2 \text{ s}^{-1}$. The simulations in section 5 account for ellipsoid dynamics due to both fluid flow and Brownian motion.

4. Feedback control of the object's position and orientation

In the presence of Brownian motion of the ellipsoid, one can control the motion of the ellipsoid by using a feedback control algorithm. This control algorithm computes the voltages that need to be applied at the electrodes so that the resultant electric field creates a flow in the device, which translates and rotates the object from the currently measured to the desired position and orientation. For any position and orientation of the object, there exists a linear map between the object's velocity and the voltages applied at the electrodes (as explained next). The necessary control electrode voltages can be computed by inverting this map, using least squares. At successive time steps, the object moves to a new position and orientation, there is a new linear map, and we solve another least squares problem to get the next set of electrode voltages. This computation can be done in real time, even for complex situations, as demonstrated in our previous experiments in which we controlled the position of multiple particles at once [5].

The desired trajectory of the ellipsoid is a series of discrete, closely spaced points in the control region with a prescribed desired orientation at each point. At each control update, the difference between the current measured position (orientation) of the object and the desired position (orientation) is multiplied by a proportionality constant called the control gain, yielding the desired (translational and angular) velocity of the object until the next control update. The controller inverts the map between the voltages and the desired translational and rotational velocities to determine the electrode voltages.

We now discuss how to compute this needed linear map, which is a composition of three individual maps related to the three physical processes that control the particle motion. In our previous experiments [5], we did not observe any significant spatial or temporal variations in the surface properties of the PDMS or glass substrates, or the viscosity of the fluid; hence we treat the zeta potential, permittivity and viscosity as spatially and temporally invariant. The first map relates the applied voltages to the resulting electric field (including the gradient of the electric field) in the control region of the device. The second relates the electric field to the fluid flow field in the device. The final map relates the flow field to the object's translational and rotational velocities. We will then show how the composition of these three maps is inverted using least squares.

For the first map, Laplace's equation for the electric potential $\nabla \cdot (\epsilon \nabla(\Phi)) = 0$ is evaluated, where ϵ is the permittivity of water and Φ is the electric potential in the domain shown in figure 5 (which contains the control region as shown in right panel of figure 2).

Eight electric fields are pre-computed, one for each channel. During operation, the electric field (or its gradient) at any point in the control region is a linear superposition of these eight electrical fields. Mathematically, this allows us to write the equations of the first map

$$\begin{pmatrix} E_{\hat{x}}(\hat{x}, \hat{y}) \\ E_{\hat{y}}(\hat{x}, \hat{y}) \\ \frac{\partial}{\partial \hat{y}}(E_{\hat{x}}(\hat{x}, \hat{y})) \\ \frac{\partial}{\partial \hat{y}}(E_{\hat{y}}(\hat{x}, \hat{y})) \end{pmatrix} = [\mathbf{A}(\hat{x}, \hat{y})] \begin{pmatrix} \eta_1 \\ \cdot \\ \cdot \\ \eta_8 \end{pmatrix}, \quad (5)$$

where η_i are the applied voltages and the matrix $\mathbf{A}(\hat{x}, \hat{y})$ (of size 4×8) is known for each point (\hat{x}, \hat{y}) in the control region using the pre-computed fields.

From equation (1), the fluid velocity at any point in the control region is directly proportional to the electric field. The flow velocity is assumed to reach steady state instantaneously after the potential difference is applied⁸ at the electrodes. The fluid shear (spatial gradient of the velocity) is directly proportional to the gradient of the electric field at that point, which gives the second map, between the electric field in the device and the resulting flow and shear field,

$$\begin{aligned} \hat{u}(\hat{x}, \hat{y}) &= \frac{\epsilon \zeta}{\mu} \cdot E_{\hat{x}}(\hat{x}, \hat{y}), \\ \hat{v}(\hat{x}, \hat{y}) &= \frac{\epsilon \zeta}{\mu} \cdot E_{\hat{y}}(\hat{x}, \hat{y}), \\ \frac{\partial}{\partial \hat{y}}(\hat{u}(\hat{x}, \hat{y})) &= \frac{\epsilon \zeta}{\mu} \cdot \frac{\partial}{\partial \hat{y}}(E_{\hat{x}}(\hat{x}, \hat{y})), \\ \frac{\partial}{\partial \hat{y}}(\hat{v}(\hat{x}, \hat{y})) &= \frac{\epsilon \zeta}{\mu} \cdot \frac{\partial}{\partial \hat{y}}(E_{\hat{y}}(\hat{x}, \hat{y})). \end{aligned} \quad (6)$$

If the ellipsoid's center of mass is at the point (\hat{x}, \hat{y}) , then the four relations in equation (6) for the fluid's velocity and the shear at (\hat{x}, \hat{y}) are the only ones needed for the third map, which relates the fluid's velocity and shear to the object's translational and rotational velocities by equations (2) and (4).

After combining the three maps, the object's translational velocities $U_{\hat{x}}$, $U_{\hat{y}}$ and its rotational velocity $\omega_{\hat{z}}$ are given by the final composite linear map

$$\begin{pmatrix} U_{\hat{x}} \\ U_{\hat{y}} \\ \omega_{\hat{z}} \end{pmatrix} = \frac{\epsilon \zeta}{\mu} \cdot \begin{pmatrix} 1 & 0 & 0 & 0 \\ 0 & 1 & 0 & 0 \\ 0 & 0 & F_c(\theta) & F_s(\theta) \end{pmatrix} [\mathbf{A}(\hat{x}, \hat{y})] \begin{pmatrix} \eta_1 \\ \cdot \\ \cdot \\ \eta_8 \end{pmatrix}, \quad (7)$$

where η_i are the applied voltages and $F_c(\theta)$ and $F_s(\theta)$ are given by $F_c(\theta) = \frac{1-e^2}{1+e^2} \cos(2\theta)$ and $F_s(\theta) = \frac{1-e^2}{1+e^2} \sin(2\theta)$. We now show how best to select the eight electrode voltages to achieve

⁸ The time T_{ss} required to reach steady state is given by $T_{ss} = \left(\frac{\log(100)}{\pi^2}\right) \cdot \frac{\rho h^2}{\mu}$, where h and ρ are the height of the channel and the density of the fluid, respectively, as derived in [36]. T_{ss} equals 0.32 ms in the device, which is much less than the control update interval of 10 ms that is typically used in our flow control device. No discernible time lag in fluid actuation was observed in previous, position control experiments [5] in our group. Hence, we assume that the flow velocity reaches steady state as soon as the voltages are applied.

the desired object velocities $U_{\hat{x}}$, $U_{\hat{y}}$ and $\omega_{\hat{z}}$ that will translate and rotate the object from where it was to where it should be (a similar argument will hold for the general case of N electrodes in an N -channel device).

At every control update, we request the desired translational and rotational velocities of the object, which are uncoupled in the case of orthotropic particles like the ellipsoid, to be, respectively, proportional to the positional and orientational deviations from the desired trajectory. These deviations, or errors, from the desired path are $\varepsilon_{\hat{x}} = \hat{x}_{\text{des}} - \hat{x}$, $\varepsilon_{\hat{y}} = \hat{y}_{\text{des}} - \hat{y}$ and $\varepsilon_{\theta} = \theta_{\text{des}} - \theta$, so $(\varepsilon_{\hat{x}}, \varepsilon_{\hat{y}})$ is the difference between the desired and current object positions and ε_{θ} is the difference between the desired and current object orientations. The desired object velocities $U_{\hat{x}}$, $U_{\hat{y}}$ and $\omega_{\hat{z}}$ are set to be proportional to the errors $\varepsilon_{\hat{x}}$, $\varepsilon_{\hat{y}}$ and ε_{θ} by the proportionality gain matrix \mathbf{K}_{prop}

$$\begin{pmatrix} U_{\hat{x}} \\ U_{\hat{y}} \\ \omega_{\hat{z}} \end{pmatrix}_{\text{des}} = \mathbf{K}_{\text{prop}} \begin{pmatrix} \varepsilon_{\hat{x}} \\ \varepsilon_{\hat{y}} \\ \varepsilon_{\theta} \end{pmatrix} = \begin{pmatrix} K_r & 0 & 0 \\ 0 & K_r & 0 \\ 0 & 0 & K_{\theta} \end{pmatrix} \begin{pmatrix} \varepsilon_{\hat{x}} \\ \varepsilon_{\hat{y}} \\ \varepsilon_{\theta} \end{pmatrix}. \quad (8)$$

The gains K_r and K_{θ} are penalties on the translational and orientational errors, respectively. A higher value of K_r forces the controller to select voltages that will translate the object to the desired position more quickly. Similarly, a higher value of K_{θ} forces the controller to select voltages that will rotate the object to the desired orientation quicker. The relative values of K_r and K_{θ} decide whether the controller spends more of its control authority on the object's translation or on its rotation.

Combining equations (7) and (8), there are more unknowns (the actuator voltages $\vec{\eta} = (\eta_1 \eta_2 \cdots \eta_8)^T$) than there are known quantities (the desired velocities $U_{\hat{x}}$, $U_{\hat{y}}$ and $\omega_{\hat{z}}$). A least square solution, which chooses the minimal size control that achieves the desired velocities, is used to find $\vec{\eta}$. Denote the linear map of equation (7) by the matrix $\mathbf{P}(\hat{x}, \hat{y})$

$$\mathbf{P}(\hat{x}, \hat{y}) = \frac{\varepsilon_{\zeta}}{\mu} \cdot \begin{pmatrix} 1 & 0 & 0 & 0 \\ 0 & 1 & 0 & 0 \\ 0 & 0 & F_c(\theta) & F_s(\theta) \end{pmatrix} [\mathbf{A}(\hat{x}, \hat{y})]. \quad (9)$$

The least square fit computes the voltages η_i , which minimize the 2-norm [37] of the electrode voltages $\|\vec{\eta}\|_2$. The optimal voltages are given by

$$\begin{pmatrix} \eta_1 \\ \cdot \\ \cdot \\ \eta_8 \end{pmatrix} = \mathbf{P}^+(\hat{x}, \hat{y}) \mathbf{K}_{\text{prop}} \begin{pmatrix} \varepsilon_{\hat{x}} \\ \varepsilon_{\hat{y}} \\ \varepsilon_{\theta} \end{pmatrix}, \quad (10)$$

where $\mathbf{P}^+(\hat{x}, \hat{y}) = (\mathbf{P}^T(\hat{x}, \hat{y})\mathbf{P}(\hat{x}, \hat{y}))^{-1}\mathbf{P}^T(\hat{x}, \hat{y})$ is the pseudo-inverse [37] of the matrix $\mathbf{P}(\hat{x}, \hat{y})$ and $\mathbf{P}^T(\hat{x}, \hat{y})$ is the transpose of the matrix $\mathbf{P}(\hat{x}, \hat{y})$. This is the control law—it states how to compute the electrode voltages given the difference between the actual and desired ellipsoid positions and orientations.

As for the control design in our previous experimental work [5], in order to avoid electrolysis (the formation of bubbles at the electrodes that can disrupt the intended flow) we limit the voltages to a maximum value (termed the saturation voltage) $\eta_{\text{sat}} = 0.15$ V. Hence, the voltages determined in equation (10) are linearly scaled so that this constraint is not violated. If the maximum absolute value of the eight voltages η_i , computed by the controller in equation (10), is η_{max} , then the eight scaled voltages η_i^{scaled} that are eventually applied at the

electrodes are given by

$$\eta_i^{\text{scaled}} = \left(\frac{\eta_{\text{sat}}}{\eta_{\text{max}}} \right) \eta_i \quad (1 \leq i \leq 8). \quad (11)$$

Since the ellipsoid velocity is linearly proportional to the applied voltages, this scaling limits the magnitude of the maximum achievable translational and rotational velocities of the object. At every time step this scaling might reduce the magnitude of the object's velocity but not the direction (even after voltage scaling, the particle is steered to correct for the deviation from the desired path, but possibly at a lower speed).

4.1. Non-dimensionalized equations for the feedback loop

A non-dimensionalized version of the governing equations using the flow Peclet numbers is presented here. The relevant physical parameters governing the dynamics are the length scales given by the radius of the control region of the device r_{dev} (in figure 5, r_{dev} is the distance from the center of the control region to the midpoint of any straight edge at the boundary), the saturation voltage η_{sat} , the zeta potential ζ at the fluid–PDMS interface and the fluid's permittivity ϵ and viscosity μ . In what follows, the non-dimensional parameters are superscripted with an asterisk.

Since the electric field in the device scales as $\frac{\eta_{\text{sat}}}{r_{\text{dev}}}$, the translational velocity V_{EOF} due to EOF will scale as $V_{\text{EOF}} = \left(\frac{\epsilon \zeta}{\mu} \right) \left(\frac{\eta_{\text{sat}}}{r_{\text{dev}}} \right)$. The time needed for the particle to traverse the control region will then scale as $t_{\text{dev}} = \frac{r_{\text{dev}}}{V_{\text{EOF}}}$. The electro-osmotic shear σ_{EOF} generated in the device will scale proportionally to the gradient of the electric field. Since the gradient of the electric field in the control region scales as $\frac{\eta_{\text{sat}}}{r_{\text{dev}}^2}$, the shear will scale as $\sigma_{\text{EOF}} = \left(\frac{\epsilon \zeta}{\mu} \right) \left(\frac{\eta_{\text{sat}}}{r_{\text{dev}}^2} \right)$, so $\sigma_{\text{EOF}} = \frac{1}{t_{\text{dev}}}$. This scaling of V_{EOF} and σ_{EOF} ignores the contribution of the shape of the control region, which is fixed once the number channels and the ratio $\frac{c_{\text{dev}}}{r_{\text{dev}}}$ are fixed (c_{dev} , the channel width, is the width of the straight edge at the boundary of the control region in figure 5). For the rest of this paper, as shown in figure 5, the number of channels is fixed at 8 and $\frac{c_{\text{dev}}}{r_{\text{dev}}}$ at 0.5.

The non-dimensional displacement and time parameters are chosen as $\hat{x}^* = \hat{x}/r_{\text{dev}}$, $\hat{y}^* = \hat{y}/r_{\text{dev}}$, $\theta^* = \theta$ and $t^* = t/t_{\text{dev}}$. The translational $[\hat{u}(\hat{x}, \hat{y}), \hat{v}(\hat{x}, \hat{y})]$ and shear components $[\frac{\partial \hat{u}(\hat{x}, \hat{y})}{\partial \hat{y}}, \frac{\partial \hat{v}(\hat{x}, \hat{y})}{\partial \hat{y}}]$ of the flow field and their non-dimensional counterparts $[\hat{u}(\hat{x}, \hat{y})^*, \hat{v}(\hat{x}, \hat{y})^*]$ and $[(\frac{\partial \hat{u}(\hat{x}, \hat{y})}{\partial \hat{y}})^*, (\frac{\partial \hat{v}(\hat{x}, \hat{y})}{\partial \hat{y}})^*]$ are related by $\hat{u}(\hat{x}, \hat{y}) = V_{\text{EOF}} \cdot \hat{u}(\hat{x}, \hat{y})^*$, $\hat{v}(\hat{x}, \hat{y}) = V_{\text{EOF}} \cdot \hat{v}(\hat{x}, \hat{y})^*$, $\frac{\partial \hat{u}(\hat{x}, \hat{y})}{\partial \hat{y}} = \sigma_{\text{EOF}} \cdot (\frac{\partial \hat{u}(\hat{x}, \hat{y})}{\partial \hat{y}})^*$ and $\frac{\partial \hat{v}(\hat{x}, \hat{y})}{\partial \hat{y}} = \sigma_{\text{EOF}} \cdot (\frac{\partial \hat{v}(\hat{x}, \hat{y})}{\partial \hat{y}})^*$. With the non-dimensional map $\mathbf{A}(\hat{x}, \hat{y})^*$ chosen as

$$\mathbf{A}(\hat{x}, \hat{y})^* = \begin{pmatrix} r_{\text{dev}} & 0 & 0 & 0 \\ 0 & r_{\text{dev}} & 0 & 0 \\ 0 & 0 & r_{\text{dev}}^2 & 0 \\ 0 & 0 & 0 & r_{\text{dev}}^2 \end{pmatrix} \mathbf{A}(\hat{x}, \hat{y}), \quad (12)$$

the non-dimensional flow components can then be stated in terms of $\mathbf{A}(\hat{x}, \hat{y})^*$ as

$$\begin{pmatrix} \hat{u}(\hat{x}, \hat{y})^* \\ \hat{v}(\hat{x}, \hat{y})^* \\ \left(\frac{\partial \hat{u}(\hat{x}, \hat{y})}{\partial \hat{y}} \right)^* \\ \left(\frac{\partial \hat{v}(\hat{x}, \hat{y})}{\partial \hat{y}} \right)^* \end{pmatrix} = \mathbf{A}(\hat{x}, \hat{y})^* \begin{pmatrix} \eta_1^* \\ \cdot \\ \cdot \\ \eta_8^* \end{pmatrix}, \quad (13)$$

where the non-dimensional voltages η_i^* are given by $\eta_i^* = \eta_i^{\text{scaled}}/\eta_{\text{sat}}$ with η_i^{scaled} chosen according to the control law given by equations (10) and (11).

The motion of the ellipsoid is governed by e_1^* ($= \frac{a_1}{r_{\text{dev}}}$), e ($= \frac{a_2}{a_1}$) and the rotational Peclet number $Pe_\theta = \sigma_{\text{EOF}}/D_\theta$ where D_θ , is the rotational diffusion coefficient about \hat{z} . Since the expected time for the ellipsoid to rotate by 1 radian about \hat{z} due to diffusion and the applied actuation are $\frac{1}{2D_\theta}$ and $\frac{1}{\sigma_{\text{EOF}}}$, respectively, the quantity Pe_θ compares the actuation's ability to compensate for the rotational diffusive motion [38]. A larger value of Pe_θ signifies a higher ability of the actuation to compensate for the diffusive motion about \hat{z} . Denoting the translational diffusion coefficients along the major and minor axes of the ellipsoid by D_x and D_y , respectively, we define two functions, $T_x^\theta(e) = \frac{D_x}{a_1^2 D_\theta}$ and $T_y^\theta(e) = \frac{D_y}{a_2^2 D_\theta}$, both of which depend solely on the parameter e (see section B.1 of the supplementary information, available from stacks.iop.org/NJP/13/013027/mmedia for details). The function $T_x^\theta(e)$ is the ratio of the expected time taken for an ellipsoid to rotate by 1 radian due to rotational diffusion about \hat{z} , to the expected time taken by the ellipsoid to diffuse by a distance a_1 along the major axis of the ellipsoid. Similarly, $T_y^\theta(e)$ is the ratio of the expected rotational diffusion time, to the expected time taken to diffuse by a distance a_2 along the minor axis of the ellipsoid.

With the control law given by equations (8) and (10), the controlled dynamics of an ellipsoid, including the effect of Brownian motion, is as follows. The geometric center translates by an amount $d\hat{x}^*$ along \hat{x}^* , $d\hat{y}^*$ along \hat{y}^* , while the ellipsoid rotates by an amount $d\theta^*$ about \hat{z} in time dt^* according to the stochastic dynamics update given by

$$\begin{aligned} d\hat{x}^* &= \hat{u}(\hat{x}, \hat{y})^* \cdot dt^* + dB_{\hat{x}}^*, \\ d\hat{y}^* &= \hat{v}(\hat{x}, \hat{y})^* \cdot dt^* + dB_{\hat{y}}^*, \\ d\theta^* &= \frac{1-e^2}{1+e^2} \left[\left(\frac{\partial \hat{u}(\hat{x}, \hat{y})}{\partial \hat{y}} \right)^* \cos(2\theta^*) + \left(\frac{\partial \hat{v}(\hat{x}, \hat{y})}{\partial \hat{y}} \right)^* \sin(2\theta^*) \right] \cdot dt^* + dB_\theta^*, \end{aligned} \quad (14)$$

where $dB_{\hat{x}}^*$ and $dB_{\hat{y}}^*$ are the translational Brownian displacements along \hat{x} and \hat{y} , respectively, and dB_θ^* is the rotational Brownian displacement about \hat{z} , which are given by

$$\begin{aligned} dB_{\hat{x}}^* &= \left(\sqrt{\frac{2T_x^\theta(e) dt^*}{Pe_\theta}} e_1^* \cos(\theta^*) - \sqrt{\frac{2T_y^\theta(e) dt^*}{Pe_\theta}} e_2^* \sin(\theta^*) \right) \cdot \mathcal{N}_x(0, 1), \\ dB_{\hat{y}}^* &= \left(\sqrt{\frac{2T_x^\theta(e) dt^*}{Pe_\theta}} e_1^* \sin(\theta^*) + \sqrt{\frac{2T_y^\theta(e) dt^*}{Pe_\theta}} e_2^* \cos(\theta^*) \right) \cdot \mathcal{N}_y(0, 1), \\ dB_\theta^* &= \left(\sqrt{\frac{2 dt^*}{Pe_\theta}} \right) \cdot \mathcal{N}_\theta(0, 1), \end{aligned} \quad (15)$$

where $e_2^* = a_2/r_{\text{dev}} = e_1^* \cdot e$. The factors $\mathcal{N}_x(0, 1)$, $\mathcal{N}_y(0, 1)$ and $\mathcal{N}_\theta(0, 1)$ denote independent Gaussian random variables with mean 0 and variance 1 which reflect the random character of Brownian motion (see [39] for an introduction to stochastic update formulae). Equations (10)–(15) describe the controlled motion of the ellipsoid in non-dimensional terms. We simulate this motion for different ellipsoid manipulation tasks and Peclet numbers in the next section.

Table 1. Examples of parameter values for $e_1^* = 0.05$, $e = 0.02$ and $Pe_\theta = 30$.

Parameter	Description	Value
ζ	Zeta potential at water–PDMS interface	5×10^{-2} V
μ	Viscosity of water	8.9×10^{-4} Pa s
T	Temperature	300 K
ϵ	Permittivity of water	$78.4 \epsilon_0$ [40]
r_{dev}	Radius of control region	100 μm
η_{sat}	Saturation voltage	1.5×10^{-1} V
t_{dev}	Time scale	1.7 s
V_{EOF}	Electro-osmotic velocity	$58 \mu\text{m s}^{-1}$
σ_{EOF}	Electro-osmotic shear	0.58 rad s^{-1}
a_1	Major axis length of ellipsoid	5 μm
$a_2(= a_3)$	Minor axis length of ellipsoid	100 nm

5. Numerical simulations of an ellipsoid's manipulation

In this section, the control law described previously is used to simulate the steering of an ellipsoid along a desired trajectory, while the ellipsoid is being perturbed by Brownian motion (according to the controlled ellipsoid dynamics described in equations (10)–(15)). We show how the ellipsoid can be translated and simultaneously rotated as well as rotated in place while trapped at a given location. We will show the dependence of the root mean square (rms) orientation error (while the ellipsoid is trapped) on Pe_θ and the shape parameter e . We explain the source of this error in detail with a simple Fokker–Planck model which can be used to theoretically predict the trapping error in orientation given the size and aspect ratio of the rod and the flow parameters.

For showing control over different trajectories, the simulations were performed with parameters $e_1^* = .05$, $e = .02$ and $Pe_\theta = 30$. Table 1 states a sample set of values of the physical parameters that reflect the above non-dimensional numbers.

Unless otherwise stated, the non-dimensional simulation results are stated in degrees for rotation, the translational displacements in units of r_{dev} , time in units of t_{dev} and applied voltages in units of η_{sat} . The applied voltages are updated every $dt^* = 5.9 \times 10^{-3}$, which corresponds to the 10 ms time lag that is expected in experiments⁹. This time lag occurs due to the finite frame rate of the camera and the computational time required by the control and object vision detection algorithm. The ellipsoid's position and orientation are assumed to be perfectly known in these simulations. The choice of gain coefficients K_r and K_θ (see equation (8)) determines the extent to which the control authority is spent on controlling position versus orientation, respectively. We experimented with different values of the gain coefficients, for achieving the optimal trade-off between positional and orientational errors in simulations and settled on $\hat{K}_r = K_r * t_{\text{dev}} = 1.7 \times 10^6$ and $\hat{K}_\theta = K_\theta * t_{\text{dev}} = 8 \times 10^4$ for all the simulations shown here.

⁹ A computational time of 3.5 ms, using MATLAB (www.mathworks.com), see footnote 6, was required for previous experiments that implemented position control of spherical particles. This includes the time needed to estimate the particle position as well as the time needed to compute the control voltages. The frame rate of the Pike camera from Allied Vision Technologies (www.alliedvisiontec.com), see footnote 6, is 200 Hz at full resolution. Thus the total feedback loop time of 8.5 ms is within the 10 ms time assumed here.

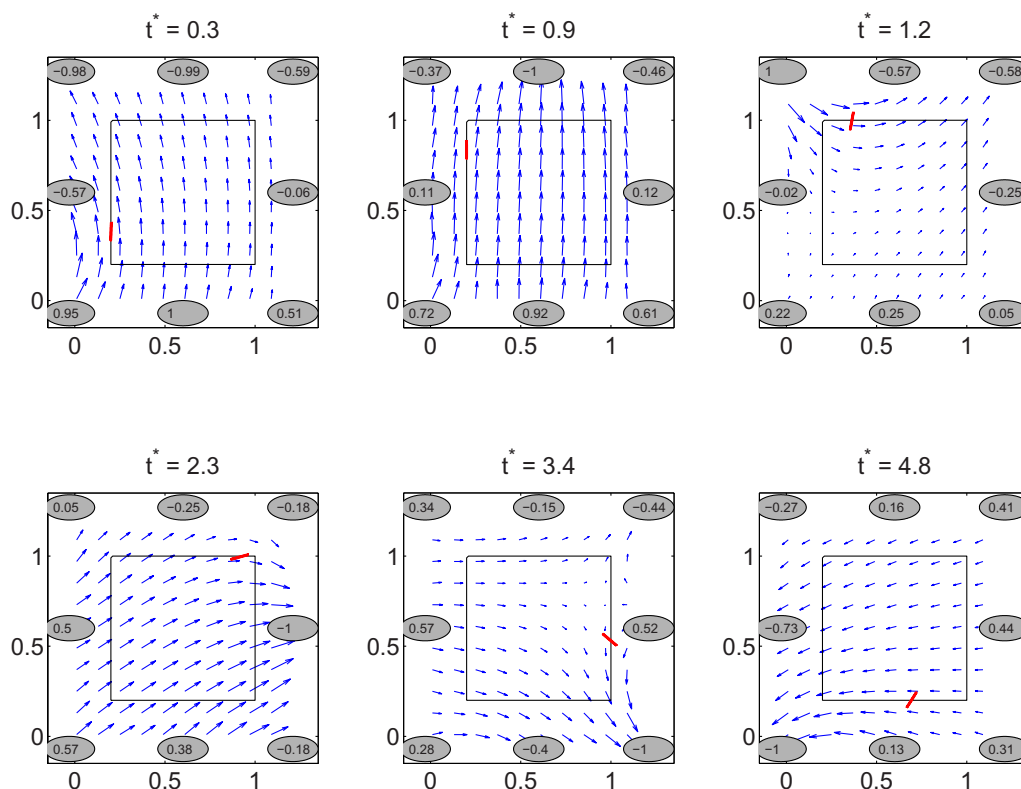


Figure 6. Six snapshots showing the ellipsoid tracing the square path (shown in black). In each snapshot, the flow field is shown with blue arrows and the voltages applied at the eight electrodes are shown inside the gray circles at the periphery. The ellipsoid is continually perturbed by Brownian motion and is controlled and corrected by the flow to start at the bottom left corner of the desired trajectory, trace the square path and then return to the bottom left corner. While traversing the trajectory from the bottom left corner to the top left corner of the square ($t^* = 0.3$ and $t^* = 0.9$), the ellipsoid is controlled to translate without rotating (an orientation of $\theta = 90^\circ$ is maintained). Then the ellipsoid is controlled to rotate by 90° while translating along each of the remaining three segments of the square. A strobe plot showing only the ellipsoid's position and orientation with respect to the square is shown in figure 7.

We will discuss the relation between η_{sat} , the rotational diffusion coefficient, and the gain coefficients at the end of this section. The first simulation is of the ellipsoid tracing a square path, shown in figures 6 and 7.

The square path has a side length equal to 0.8. The ellipsoid initially starts off at the bottom left corner of the square and is returned to the same point at the end of the simulation. In the initial part of the simulation (from the bottom left to the top left corner of the square path), the ellipsoid is controlled to move along a straight line, at a constant orientation ($\theta^* = 90^\circ$). Along the next three sides of the square, the ellipsoid is controlled to rotate by 90° by the time it reaches the end of that side (see movie M1 in supplementary information, available from stacks.iop.org/NJP/13/013027/mmedia). The positional and orientation errors are shown in figure 8.

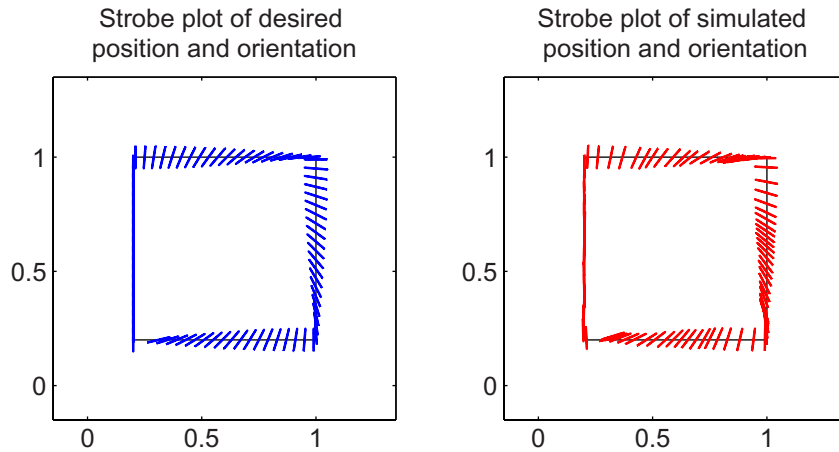


Figure 7. The panel on the left is a strobe plot of the desired orientation of the ellipsoid along different points of the square path. The panel on the right shows a strobe plot of the ellipsoid tracing the square path (shown here for 95 consecutive time steps). The side of the square path (marked in black) measures 0.8 in the non-dimensional length units. The ellipsoid starts in the bottom left corner, traces the path and returns to the starting point by $t^* = 5.6$.

In figure 9, we demonstrate the ellipsoid being controlled along a more complex ‘hour glass’ path shape that spans the entire control region. The ellipsoid starts at the bottom left corner of the trajectory at an initial orientation of $\theta^* = 90^\circ$. It is then controlled to move to the top right corner, then to the top left corner, down to the bottom right corner and finally back to the bottom left corner. While translating, the ellipsoid is controlled to simultaneously rotate so that its major axis is aligned with each of the four segments of the trajectory by the time it reaches the end of that segment (see movie M2 in supplementary information, available from stacks.iop.org/NJP/13/013027/mmedia).

The next simulation shows the ellipsoid both trapped in place and being rotated from an initial orientation of 90° to a final orientation of 0° by EOF control. The change in orientation of the ellipsoid over time and the associated flow field and electrode voltages are shown in figure 10 (see movie M3 in supplementary information).

In the initial part of the simulation (until $t^* = 1.17$), the controller spends most of its control authority on rotating the ellipsoid from $\theta = 90^\circ$ to $\theta = 0^\circ$ compared to correcting for positional error due to translational Brownian motion. This results in a nonzero mean translational error of 1.9×10^{-4} in position, with an rms of 1.3×10^{-4} . In the tail end of the above simulation, when the ellipsoid is nominally trapped at the desired location and orientation, as shown in figure 12, we observe an rms error in the orientation angle. The rms error in orientation, rms_{sim} , is computed from the simulations in the following manner:

$$\text{rms}_{\text{sim}} = \left(\frac{1}{n} \sum_{i=m}^{i=m+n} (\theta^*(t_i^*) - \bar{\theta}^*)^2 \right)^{1/2}, \quad (16)$$

where $\theta^*(t_i^*)$ is the orientation of the ellipsoid at the i th time step. There are a total of $(m+n)$ time steps in the simulation; the ellipsoid first reaches $\theta^* = 0^\circ$ at the m th time step (termed the first passage time) and then $\bar{\theta}^* = \frac{1}{n+1} (\sum_{i=m}^{i=m+n} \theta(t_i^*))$. This rms error is a result of the competition

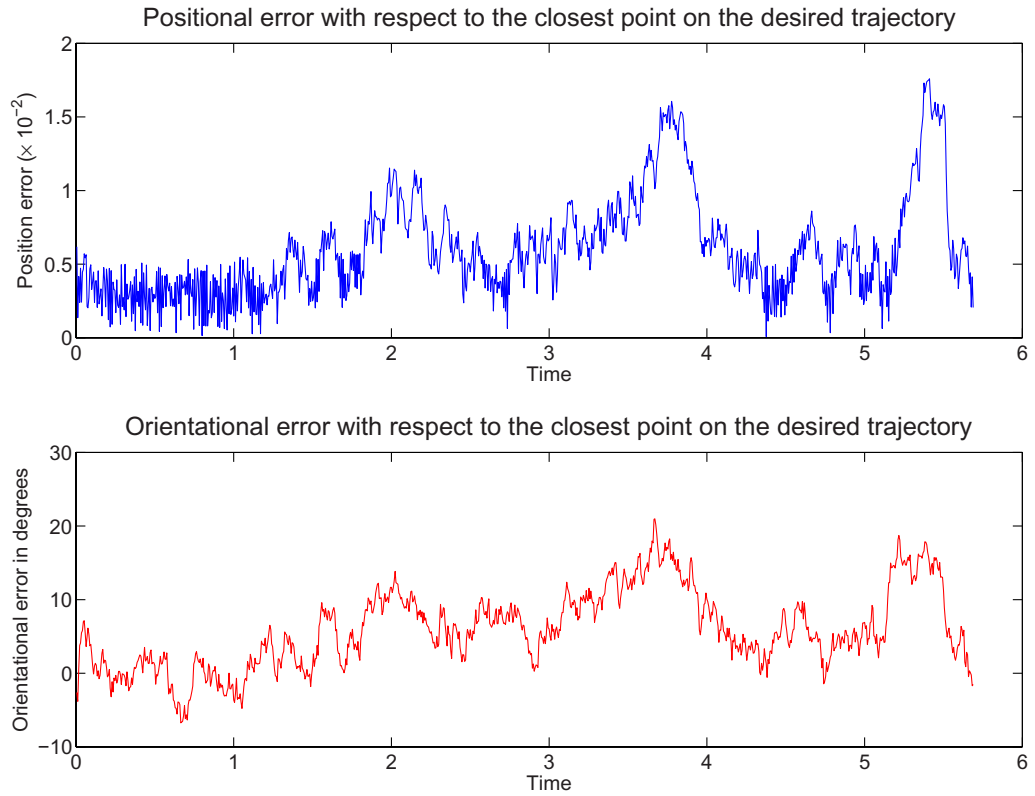


Figure 8. The top and bottom panels show the variation of the positional and orientational errors, respectively, for the ellipsoid tracing the square path. Denote the coordinates of the ellipsoid at time t_i^* by $(\hat{x}^*(t_i^*), \hat{y}^*(t_i^*), \theta^*(t_i^*))$ and the coordinates that were desired at the previous time step t_{i-1}^* by $(\hat{x}_{\text{des}}^*(t_{i-1}^*), \hat{y}_{\text{des}}^*(t_{i-1}^*), \theta_{\text{des}}^*(t_{i-1}^*))$. The positional error $\varepsilon_{\text{pos}}(t_i^*)$ is defined as $\varepsilon_{\text{pos}}(t_i^*) \equiv ((\hat{x}^*(t_i^*) - \hat{x}_{\text{des}}^*(t_{i-1}^*))^2 + (\hat{y}^*(t_i^*) - \hat{y}_{\text{des}}^*(t_{i-1}^*))^2)^{\frac{1}{2}}$. The orientational error $\varepsilon_{\theta^*}(t_i^*)$ is defined as $\varepsilon_{\theta^*}(t_i^*) \equiv \theta^*(t_i^*) - \theta_{\text{des}}^*(t_{i-1}^*)$. For the first side of the square ($0 < t^* < 1.2$), apart from countering rotational Brownian motion, there was no need to rotate the ellipsoid. Hence, the available control authority could be committed more fully to correcting positional errors. At subsequent stages, the need to turn the ellipsoid leads to a decreased capability to correct positional errors.

between Brownian motion and the controller. The rotational Brownian motion of the ellipsoid will tend to rotate the ellipsoid away from $\theta^* = 0^\circ$, while the controller tries to bring it back to $\theta^* = 0^\circ$.

Since the rotational dynamics depends on the rotational Peclet number Pe_θ and the shape parameter e , we plot the dependence of the rms trapping error as a function of these variables in figure 11. For better visualization, the error is plotted against the aspect ratio $1/e$. As one would expect, the orientation error decreases with increasing Pe_θ because of comparatively larger actuation compensating for the particle's diffusive motion. For a fixed Pe_θ , the plot shows a sharp increase in error as the aspect ratio approaches 1, i.e. as the shape of the ellipsoid approaches that of the sphere (unit aspect ratio). In addition, there is a slow increase in error, for

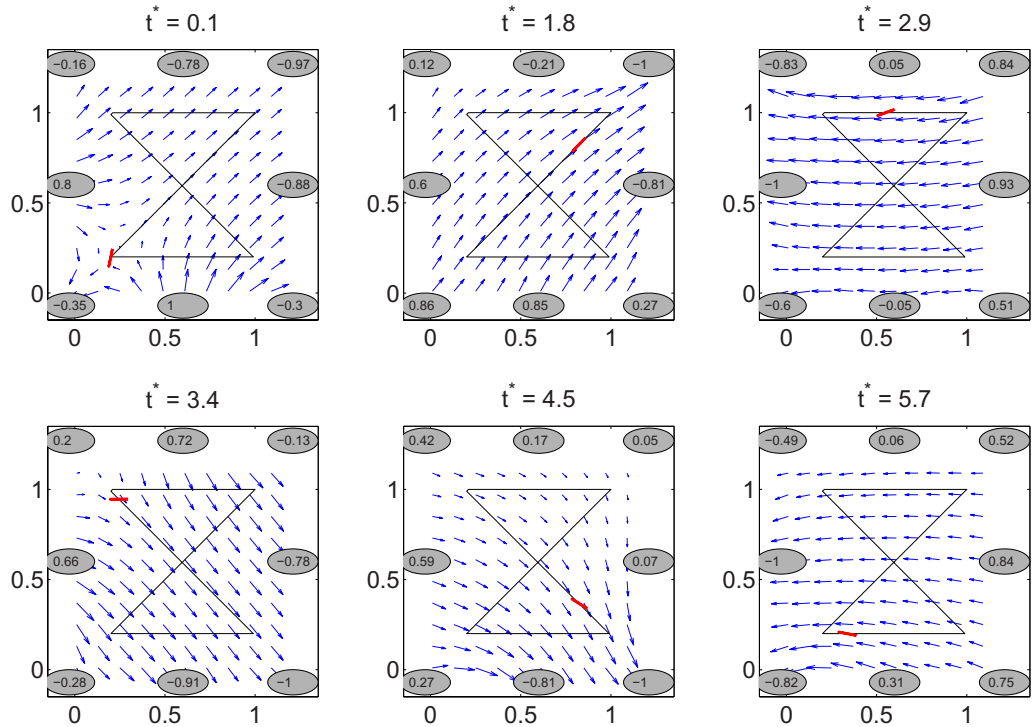


Figure 9. Six snapshots showing the ellipsoid tracing the ‘hour glass’ path (shown in black) that spans the majority of the control region. The ellipsoid starts at the bottom left corner of the desired trajectory, traces the path and then is returned to the bottom left corner. Along each of the four segments of the desired trajectory, the orientation task is to align the major axis of the ellipsoid along that segment by the time it reaches the end of that segment.

a fixed Pe_θ , as the aspect ratio increases (compare errors between aspect ratios 10 and 50). We explain this next.

5.1. The Fokker–Planck equation describing the orientation error

It is possible to theoretically estimate the variation of the rms error in orientation, termed $\text{rms}_{\text{theor}}$, with respect to the size and the aspect ratio of the ellipsoid as

$$\begin{aligned} \text{rms}_{\text{theor}} &= \sqrt{2} \left(\frac{1+e^2}{1-e^2} \right) \left(\frac{D_\theta}{\sigma_{\max}} \right) \\ &\equiv \sqrt{2} \left(\frac{1+e^2}{1-e^2} \right) \left(\frac{kT}{\mu} \right) \left(\frac{g(e)}{a_1^3} \right) \left(\frac{1}{\sigma_{\max}} \right), \end{aligned} \quad (17)$$

where $\text{rms}_{\text{theor}}$ is in radians, σ_{\max} is the maximum rotational velocity with which one can turn the ellipsoid and $D_\theta \equiv \left(\frac{kT}{\mu} \right) \frac{g(e)}{a_1^3}$ (see [35] and expressions for the rotational diffusion coefficient in section B of the supplementary information, available from stacks.iop.org/NJP/13/013027/mmedia) to see that D_θ is inversely proportional to a_1^3).

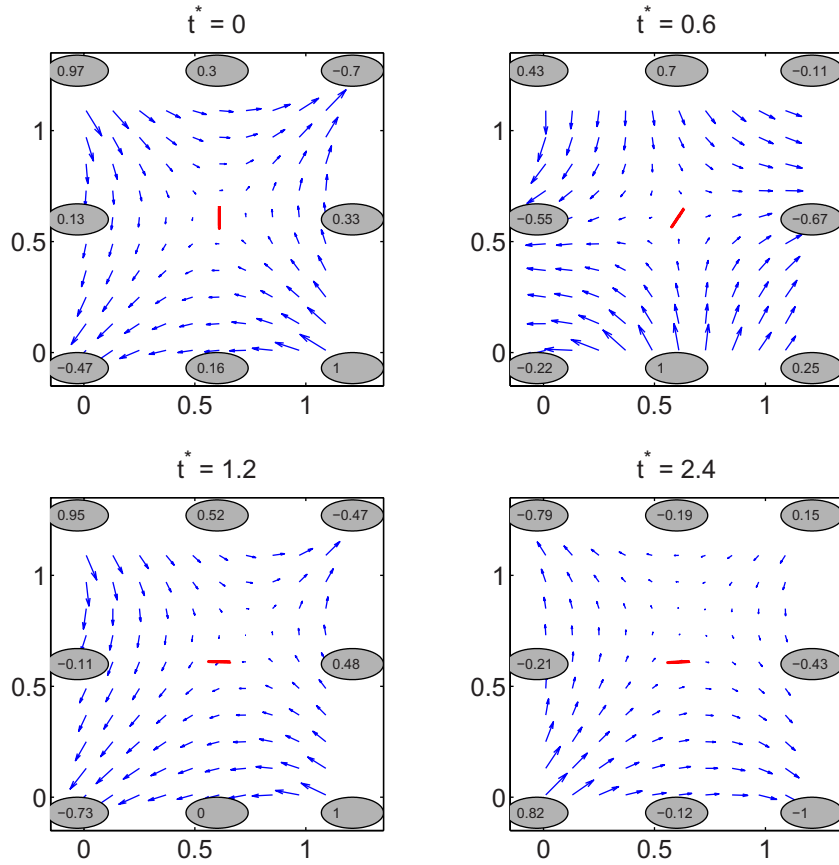


Figure 10. Four snapshots showing the ellipsoid rotating by 90° . In each snapshot, the flow field is shown with blue arrows and the voltages applied at the eight electrodes are shown inside the gray circles at the periphery. The ellipsoid has been rotated by 90° by $t^* = 1.2$ after which the controller continuously adjusts voltages to counteract Brownian motion and maintain the ellipsoid in place at $\theta^* = 0^\circ$.

The value of σ_{\max} equals the maximum allowable fluid shear that can be actuated by the electrodes under the constraint that the applied voltages do not exceed η_{sat} . In terms of Pe_θ , equation (17) can be rewritten as

$$\text{rms}_{\text{theor}} = \sqrt{2} \left(\frac{1+e^2}{1-e^2} \right) \left(\frac{1}{\sigma_{\max}^* Pe_\theta} \right), \quad (18)$$

where σ_{\max}^* is the non-dimensional maximum shear that only depends on the shape of the device, i.e. on the number of channels and the device geometry parameter $\frac{c_{\text{dev}}}{r_{\text{dev}}}$.

A derivation of the expression in equation (17) makes use of two observations noted in the simulations. Firstly, the controller spends most of its control authority in maintaining the ellipsoid's orientation at $\theta = 0^\circ$ and relatively less authority on position control. Secondly, as seen in the bottom panel of figure 12 (which corresponds to $e_1^* = 0.05$, $e = 0.02$ and $Pe_\theta = 30$), the controller exerts this authority by maintaining the value of the shear component $(\frac{\partial \hat{u}}{\partial \hat{y}})^*$ at

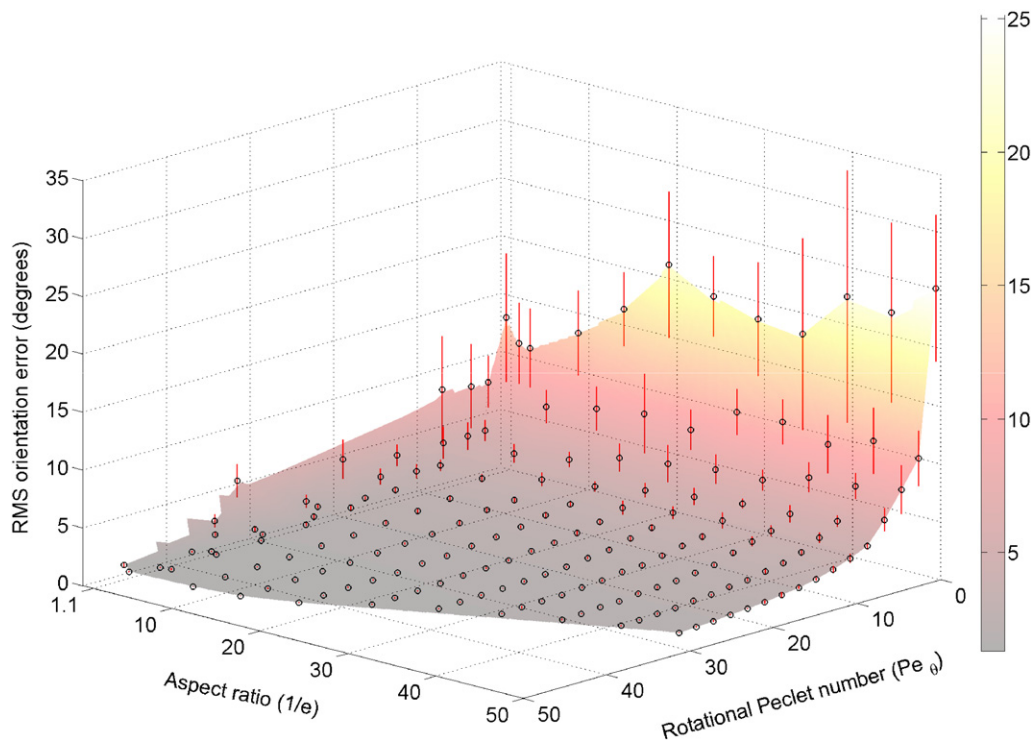


Figure 11. Effect of aspect ratio and rotational Peclet number on rms orientation error: the parameter e_1^* , which corresponds to the semi-major axis length of the ellipsoid, was fixed at the value 0.05. For each (Pe_θ, e) , the plotted values are the average of 10 runs of the simulation with the ellipsoid being nominally trapped at 0° . The error bar for each average is plotted on the graph, while a surface is fitted to the data to guide the eye. Increasing values of Pe_θ means that more shear is available to compensate for the perturbation due to the rotational Brownian motion of the ellipsoid, thus decreasing the error. For a fixed Pe_θ , there is a sharp increase in error as the shape of the ellipsoid approaches that of the sphere (aspect ratio ≈ 1.1). This effect is explained in the text.

the maximum of ± 1.6 for most time steps after $t^* \approx 1.1$ (when it is first oriented at $\theta^* = 0^\circ$). It abruptly switches between ± 1.6 as needed in order to counteract the rotational Brownian motion of the ellipsoid. Thus, the controller essentially executes a simple *bang–bang*-type control law [41] for maintaining the ellipsoid’s orientation at $\theta^* = 0^\circ$: it checks whether the ellipsoid has positive orientation $\theta^* > 0^\circ$, or negative orientation, $\theta^* < 0^\circ$, and attempts to apply the maximum allowable shear ($\sigma_{\max}^* = 1.6$), which can rotate the ellipsoid back to $\theta^* = 0^\circ$. The associated Fokker–Planck equation for the probability distribution function of θ that arises from the stochastic differential equation that describes the above simplified control law yields equation (17), as explained in detail in section C of the supplementary information (available from stacks.iop.org/NJP/13/013027/mmedia).

In figure 13, we compare $\text{rms}_{\text{theor}}$ and rms_{sim} for a range of ellipsoid sizes a_1 and aspect ratios $\frac{a_1}{a_2}$ (note: $e = \frac{a_2}{a_1}$). The simulations for computing rms_{sim} were performed with the flow parameters stated in table 1, with the ellipsoid being trapped by EOF control at the center of the control region. For plotting $\text{rms}_{\text{theor}}$, we set the maximum shear, which is a property of

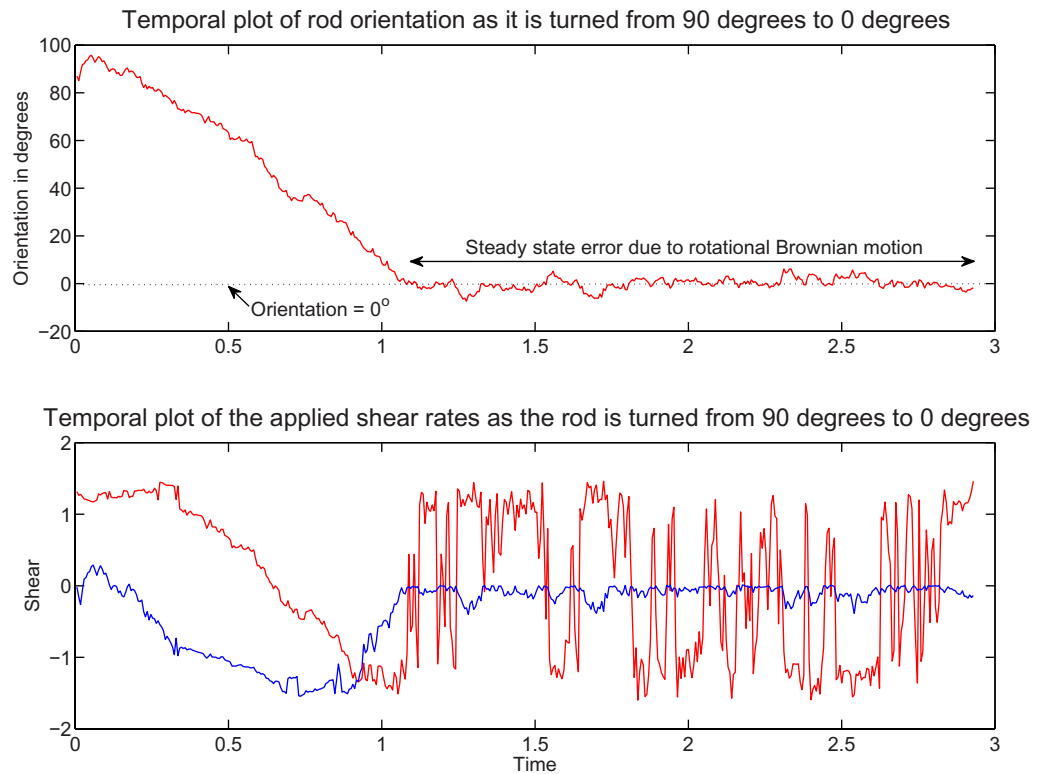


Figure 12. The top panel shows the temporal trace of the ellipsoid's orientation as it is being turned by 90°. The bottom panel shows the temporal trace of the 'unperturbed' fluid shear rates, $(\frac{\partial \hat{u}}{\partial \hat{y}})^*$ in red and $(\frac{\partial \hat{v}}{\partial \hat{y}})^*$ in blue, computed at the geometric center of the ellipsoid. For most of the time steps after $t^* = 1.2$, the controller can be seen to maintain the value of the shear component $(\frac{\partial \hat{u}}{\partial \hat{y}})^*$ at the maximum it can create, ± 1.62 , or it abruptly switches between these values. This switching counteracts the rotational Brownian motion of the ellipsoid and maintains its orientation at $\theta^* = 0^\circ$.

the device/controller and not the ellipsoid, as $\sigma_{\max} = 0.94 \text{ rad s}^{-1}$ (corresponding to $\sigma_{\max}^* = 1.6$ shown in figure 12). Given that we disregard any loss of control authority for position control in the simple model of the control law that was used to derive $\text{rms}_{\text{theor}}$, the good match between rms_{sim} and $\text{rms}_{\text{theor}}$ for the range of particle sizes and aspect ratios under consideration verifies that most of the controller's authority is indeed spent in controlling the orientation rather than the position of the ellipsoid.

For a fixed aspect ratio, the rotational diffusion coefficient varies inversely as a_1^3 (as opposed to the translational diffusion coefficient, which is inversely proportional to a_1). Hence as a_1 decreases, the rms error should increase as seen in figure 13. The increase in aspect ratio $(\frac{a_1}{a_2})$, for fixed a_1 , causes a comparatively weaker increase in the diffusion coefficient and consequently in the rms error. For a fixed a_1 , the aspect ratio-dependent term $\frac{1+e^2}{1-e^2}$ (in equation (17)) increases the rms error as $e \rightarrow 1$. This is observed in figure 13, more noticeably for smaller particles, at $\frac{a_1}{a_2} = 1.1$. This increase in rms error reflects the loss in the ability of a curl-free flow to rotate a near-spherical-shaped particle.

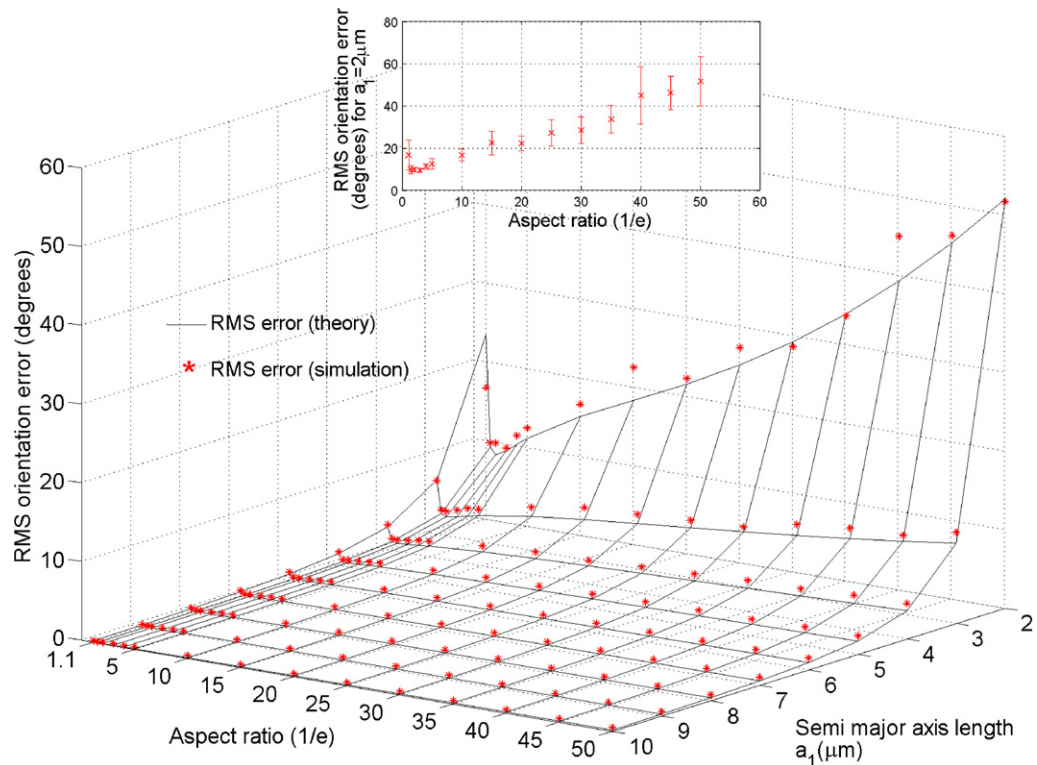


Figure 13. Comparison of rms errors in orientation between the theoretical estimate $\text{rms}_{\text{theor}}$ (equation (17)) and the simulation-based estimate rms_{sim} (equation (16)) for flow parameters stated in table 1. For each ellipsoid size and aspect ratio, the plotted value of rms_{sim} is the average of 10 runs of the simulation with each run lasting 50 s while the ellipsoid was trapped at the center of the control region. The error bars for the simulation-based estimate rms_{sim} are shown in the inset for $a_1 = 2 \mu\text{m}$, while the error bars for other values of a_1 are too small to depict on the plot. The plot shows the rms as the ellipsoid size (a_1) decreases. For a fixed a_1 , the plot shows an increase in rms error at the highest and lowest values of the aspect ratios ($\frac{a_1}{a_2}$) with a dip in rms error at $\frac{a_1}{a_2} \approx 2$. The diffusion coefficient increases weakly with aspect ratio. Consequently, for a fixed size a_1 , there is a comparatively slow increase in rms error seen for values $\frac{a_1}{a_2} > 5$ in the plot. As the aspect ratio decreases ($\frac{a_1}{a_2} \rightarrow 1$), there is a sharper increase in rms error due to the term $\frac{1+e^2}{1-e^2}$ in equation (17). This effect is noticeable for smaller ellipsoids ($a_1 \leq 3 \mu\text{m}$). The good match between $\text{rms}_{\text{theor}}$ and rms_{sim} shows that orientation control is harder to achieve and so the controller spends most of its authority in controlling orientation rather than position. The ellipsoid size $a_1 = 3 \mu\text{m}$ and the aspect ratio $\frac{a_1}{a_2} = 1.2$ are seen to be lower bounds for maintaining an rms error of 5° .

In another work by our group [6], we have been able to experimentally show position control of nanoscopic particles by EOF-based position control in a highly viscous fluid. This was possible because the actuation was not saturated while trying to control the particle position but the increased viscosity reduced the translation diffusion coefficient. However, this avenue is not

feasible for orientation control because the actuation does saturate while trying to compensate for rotational diffusion. Thus the effectiveness of rotational control is set by actuator saturation. The rotational Peclet number Pe_θ is independent of fluid viscosity. Seen in dimensional terms, the rotational diffusion coefficient D_θ as well as the maximum shear σ_{\max} (which was set as the maximum value of the fluid shear $\frac{\partial}{\partial \hat{y}}(\hat{u})$ observed in figure 12) are both inversely proportional to the fluid viscosity (see equation (11) in section B of the supplementary information, available from stacks.iop.org/NJP/13/013027/mmedia, for an expression of the diffusion coefficient and equation (6) in the main text for the shear field). Hence, increasing the fluid viscosity does not decrease the value of the rms error in orientation (since $\text{rms}_{\text{theor}} \approx D_\theta/\sigma_{\max}$). Thus, in the control model described in this paper, for the flow parameters stated in table 1, even though slender particles (where $a_2 = 100$ nm for example) can be controlled, $a_1 = 3$ μm and $\frac{a_1}{a_2} = 1.2$ are seen to be lower bounds on the particle size and aspect ratio for maintaining rms errors in orientation of around 5° , irrespective of the fluid viscosity. Since the control voltages are not allowed to exceed η_{sat} penalizing the orientation error in equation (10) by indefinitely increasing the control gain K_θ does not reduce the orientation error below what is allowable by the maximum shear σ_{\max} . Instead one could reduce electrolysis at the electrodes by protecting them with a film of nafion [42]. This would allow for an increased value of η_{sat} , and hence an increased value of σ_{\max} , thus reducing the rms error. This will be investigated in future experiments.

6. Additional considerations towards experiments

In this section, we consider additional features that will be important for future experiments and applications. We first consider the effect of the size and shape of more general objects for flow control. For other types of orthotropic particles, for example a cylinder, there will be a different constant, instead of $\frac{1-e^2}{1+e^2}$, that determines the rotational velocity of the particle in equation (4). This constant can be computed by simulating the flow around the cylinder with the Stokes flow equations (described in section A of the supplementary information) and integrating the resulting shear and pressure distributions on the surface of the cylinder. The cylinder's motion can be controlled using a similar control law modified with this new constant. Also in experiments, the exact size of the cylinder can only be known to a certain precision. Since the control voltages depends on the object size (through the $\mathbf{P}(\hat{x}, \hat{y})$ matrix in equation (9)) as well as on the gain matrix \mathbf{K}_{prop} in equation (10), one could compensate for the imprecise knowledge of the object size by experimenting with the value of \mathbf{K}_{prop} until a suitable performance is achieved.

For non-orthotropic particles, since translation and rotation are coupled, the structure of the $\mathbf{P}(\hat{x}, \hat{y})$ matrix will change. In particular, some of the elements of the matrix that premultiplies $\mathbf{A}(\hat{x}, \hat{y})$ in equation (9) will have a nonzero value. However, one can still compute the pseudo-inverse of $\mathbf{P}(\hat{x}, \hat{y})$ and obtain the control voltages, after one makes an appropriate choice of \mathbf{K}_{prop} . In this case, \mathbf{K}_{prop} should be chosen to be non-diagonal to ensure that orientation and position errors are penalized in a manner that accounts for the coupling between translation and rotation.

We have shown simulations in which the object is being controlled in two dimensions; however, the translational diffusion of the object in the z -direction and the rotational 'pitching' diffusion about the body-fixed y -axis can bring the object in contact with (and thus might make it stick to) the glass and PDMS surfaces that form the floor and ceiling of the device, respectively.

However, the object may have a natural electrostatic repulsion to the wall and, if not, coatings can be applied to the device that will prevent sticking of the object to the device [43]. With such coatings and by considering devices that are thin with respect to the object length, one can mitigate the tendency of the object to pitch out of the plane in which it is being controlled. Even when the object pitches out of plane, one does not completely lose the ability to control the rod in the plane of the device. As long as the pitching angle is small, one should expect to control the rotation about \hat{z} (normal to the device plane) with the same control law as proposed in this paper, with a modified rotational gain K_θ (see equation (8)).

Our control algorithm assumes that the object velocity exhibits a linear dependence on the electric field (see equations (2) and (4)). However, the object itself might have a charged Debye layer at its interface with the surrounding fluid. In the presence of an applied electric field, the ions in the Debye layer will move the local fluid surrounding the object, which can in turn impart an unintended translational and rotational velocity to the object. Such an electrophoretic motion of the particle, due to its own (uniform) zeta potential, is linearly dependent on the electric field [44] and can be readily accommodated within our control law as explained in section D of the supplementary information (available from stacks.iop.org/NJP/13/013027/mmedia).

However, depending on whether the object is strongly polarizable, one could observe a quadratic dependence of the velocity on the electric field, as opposed to the strictly linear dependence described in the previous section. This quadratic dependence is induced charge electrophoresis (ICEP) [45]–[48]. This effect is explained in section D of the supplementary information where we show that the magnitude of the rotational velocity of the ellipsoid due to ICEP using the approximations used by Saintillan *et al* [48] is negligible (less than 6% of that due to EOF) due to the low electric field strengths (less than 7 V cm^{-1}) at the ellipsoid's location in the control region. The translational velocity of the ellipsoid due to ICEP is identically zero [48]. This matches well with experimental results [49], where the rotational velocity of a comparably sized object ($6 \mu\text{m} \times 300 \text{ nm}$) in water due to ICEP was noticeable only at electric field strengths that were greater than 30 V cm^{-1} . Hence this nonlinear effect can be safely neglected in our simulations.

7. Conclusion

We have described the physics that shows how a planar electro-osmotic flow translates and rotates an object that is immersed in it. The map describing this physics can be inverted to obtain a control law that allows one to manipulate the position and orientation of the object by electrically actuating the flow. Our simulations and theoretical model show how the performance of the algorithm scales with the size and aspect ratio of an ellipsoidal object and we have explained how this approach can be extended to objects of more general shapes. In order to realize what we have discussed experimentally, we need to extend our vision algorithm to also estimate the orientation of objects. The vision algorithm has to be robust to the uncertainty in measurement due to pixelation in the camera sensor, dark noise from the camera, low photon counts if the objects are dimly fluorescent or measurement noise due to imperfect estimation of a small metallic object's orientation from its scattered light. We are currently developing the needed vision algorithms as well as implementing our control methods in hardware, to demonstrate position and orientation control of one and multiple objects simultaneously in experiments. These results will be reported in future publications.

Acknowledgments

We thank Peter Carmichael, Gregg Gallatin and Jabez McClelland, all affiliated with the Center for Nanoscale Science and Technology (CNST) at the National Institute of Standards and Technology (NIST), Gaithersburg, MD, USA and Matthew McMahon at the Naval Surface Warfare Center, West Bethesda, MD, USA (formerly at CNST), for stimulating discussions. We are grateful to Klint Rose at Lawrence Livermore National Labs, Livermore, CA, USA and Juan Santiago at Stanford University, Stanford, CA, USA for helpful discussions on induced charge electro-osmosis. We also acknowledge helpful discussions with Joseph Hubbard at NIST, Gaithersburg, MD, USA on fluid dynamics of nano-objects. The first author (PPM) was supported by the CNST–UMD cooperative grant.

References

- [1] Sirbuly D J, Law M, Yan H and Yang P 2005 Semiconductor nanowires for subwavelength photonics integration *J. Phys. Chem. B* **109** 15190–213
- [2] Messer B, Song J H and Yang P 2000 Microchannel networks for nanowire patterning *J. Am. Chem. Soc.* **122** 10232–3
- [3] Minerick A, Zhou R, Takhistov P and Chang H 2003 Manipulation and characterization of red blood cells with alternating current fields in microdevices *Electrophoresis* **24** 3703–17
- [4] Chaudhary S and Shapiro B 2006 Arbitrary steering of multiple particles independently in an electro-osmotically driven microfluidic system *IEEE Trans. Control Syst. Technol.* **14** 669–80
- [5] Armani M D, Chaudhary S V, Probst R and Shapiro B 2006 Using feedback control of microflows to independently steer multiple particles *J. Microelectromech. Syst.* **15** 945–54
- [6] Ropp C, Probst R, Cummins Z, Kumar R, Berglund A, Raghavan S R, Waks E and Shapiro B 2010 Manipulating quantum dots to nanometer precision by control of flow *Nano Lett.* **10** 2525–30
- [7] Friese M E J, Nieminen T A, Heckenberg N R and Rubinsztein-Dunlop H 1998 Optical alignment and spinning of laser-trapped microscopic particles *Nature* **394** 348–50
- [8] La Porta A and Wang M D 2004 Optical torque wrench: angular trapping, rotation and torque detection of quartz microparticles *Phys. Rev. Lett.* **92** 190801
- [9] Bingelyte V, Leach J, Courtial J and Padgett M J 2003 Optically controlled three-dimensional rotation of microscopic objects *Appl. Phys. Lett.* **82** 829–31
- [10] ONeil A T and Padgett M J 2002 Rotational control within optical tweezers by use of a rotating aperture *Opt. Lett.* **27** 743–5
- [11] Dasgupta R, Mohanty P K and Gupta P K 2003 Controlled rotation of biological microscopic objects using optical line tweezers *Biotechnol. Lett.* **25** 1625–8
- [12] Paterson L, MacDonald M P, Arlt J, Sibbett W, Bryant P E and Dholakia K 2001 Controlled rotation of optically trapped microscopic particles *Science* **292** 912–14
- [13] Neuman K C, Chadd E H, Liou G F, Bergman K and Block S M 1999 Characterization of photodamage to *Escherichia coli* in optical traps *Biophys. J.* **77** 2856–63
- [14] Zhang L, Abbott J J, Dong L, Kratochvil B E, Bell D and Nelson B J 2009 Artificial bacterial flagella: fabrication and magnetic control *Appl. Phys. Lett.* **94** 064107
- [15] Sacconi L, Romano G, Ballerini R, Capitanio M, De Pas M and Giuntini M 2001 Three-dimensional magneto-optic trap for micro-object manipulation *Opt. Lett.* **26** 1359–62
- [16] Zhang L, Abbott J J, Dong L, Peyer K E, Kratochvil B E, Zhang H, Bergeles C and Nelson B J 2009 Characterizing the swimming properties of artificial bacterial flagella *Nano Lett.* **9** 3663–7
- [17] Reich D H, Tanase M, Hultgren A, Bauer L A, Chen C S and Meyer G J 2003 Biological applications of multifunctional magnetic nanowires *J. Appl. Phys.* **93** 7275–80

- [18] Edwards B, Engheta N and Evoy S 2007 Electric tweezers: experimental study of positive dielectrophoresis-based positioning and orientation of a nanorod *J. Appl. Phys.* **102** 024913
- [19] Raychaudhuri S, Dayeh S A, Wang D and Yu E T 2009 Precise semiconductor nanowire placement through dielectrophoresis *Nano Lett.* **9** 2260–6
- [20] Hermanson K D, Lumsdon S O, Williams J P, Kaler E W and Velev O D 2001 Dielectrophoretically assisted assembly of electrically functional microwires from nanoparticle suspensions *Science* **294** 1082–6
- [21] Smith P A, Nordquist C D, Jackson T N and Mayer T S 2000 Electric-field assisted assembly and alignment of metallic nanowires *Appl. Phys. Lett.* **77** 1399–401
- [22] Jamshidi A, Pauzaskie P J, Schuck P J, Ohta A T, Chiou P, Chou J, Yang P and Wu M C 2008 Dynamic manipulation and separation of individual semiconducting and metallic nanowires *Nat. Photonics* **2** 85–9
- [23] Ahmed W, Kooij E S, van Silfhout A and Poelsema B 2009 Quantitative analysis of gold nanorod alignment after electric field-assisted deposition *Nano Lett.* **9** 3786–94
- [24] Altomare L, Borgatti M, Medoro G, Manaresi N, Tartagni M, Guerrieri R and Gambari R 2003 Levitation and movement of human tumor cells using a printed circuit board device based on software-controlled dielectrophoresis *Biotechnol. Bioeng.* **82** 474–9
- [25] Probstein R F 1994 *Physicochemical Hydrodynamics* (New York: Wiley)
- [26] Lyklema J 1991 *Fundamentals of Interface and Colloid Science: Solid–Liquid Interfaces* vol II (San Diego, CA: Academic)
- [27] Jeffery G B 1922 The motion of ellipsoidal particles immersed in a viscous fluid *Proc. R. Soc. A* **102** 161–79
- [28] Bretherton F P 1962 The motion of rigid particles in a shear flow at a low Reynolds number *J. Fluid Mech.* **14** 284–304
- [29] Brenner H 1964 The stokes resistance of an arbitrary particle—part IV. Arbitrary fields of flow *Chem. Eng. Sci.* **19** 703–27
- [30] Brenner H 1962 Effect of finite boundaries on the Stokes resistance of an arbitrary particle *J. Fluid Mech.* **12** 35–48
- [31] Padding J T and Briels W J 2010 Translational and rotational friction on a colloidal rod near a wall *J. Chem. Phys.* **132** 054511
- [32] Faxen H 1927 The velocity of two spheres that fall under the influence of gravity in a viscous fluid (Translated title) *Z. Angew. Math. Mech.* **7** 79–80
- [33] Stimson M and Jeffrey G B 1926 The motion of two spheres in a viscous fluid *Proc. R. Soc. A* **111** 110–16
- [34] Happel J and Brenner H 1965 *Low Reynolds Number Hydrodynamics* (Englewood Cliffs, NJ: Prentice-Hall)
- [35] Brenner H 1967 Coupling between the translational and rotational Brownian motions of rigid particles of arbitrary shape *J. Colloid Interface Sci.* **23** 407–36
- [36] Patankar N A and Hu H H 1998 Numerical simulation of electro-osmotic flow *Anal. Chem.* **70** 1870–81
- [37] Strang G 1988 *Linear Algebra and its Applications* (Pacific Grove, CA: Brooks Cole)
- [38] Brenner H 1970 Orientation-space boundary layers in problems of rotational diffusion and convection at large rotary Peclet numbers *J. Colloid Interface Sci.* **34** 103–25
- [39] Gillespie D T 1996 The mathematics of Brownian motion and Johnson noise *Am. J. Phys.* **64** 225–40
- [40] Lide D R 2009 *CRC Handbook of Chemistry and Physics* 90th edn (Boca Raton, FL: CRC Press)
- [41] Sonneborn L and Van Vleck F 1965 The bang-bang principle for linear control systems *SIAM J. Control* **2** 151–9
- [42] Liu F, Yi B, Xing D, Yu J and Zhang H 2003 Nafion/PTFE composite membranes for fuel cell applications *J. Membr. Sci.* **212** 213–23
- [43] Han Y, Alsayed A M, Nobili M, Zhang J, Lubensky T C and Yodh A G 2006 Brownian motion of an ellipsoid *Science* **314** 626–30
- [44] Sellier A 2002 A note on the electrophoresis of a uniformly charged particle *Q. J. Math. Appl. Mech.* **55** 561–72

- [45] Gamayunov N I, Murtsovkin V A and Dukhin A S 1986 Pair interaction of particles in electric field—1. Features of hydrodynamic interactions of polarized particles *Colloid J. USSR* **48** 197–203
- [46] Squires T M and Bazant M Z 2006 Breaking symmetries in induced-charge electro-osmosis and electrophoresis *J. Fluid Mech.* **560** 65–101
- [47] Yariv E 2005 Induced-charge electrophoresis of nonspherical particles *Phys. Fluids* **17** 051702
- [48] Saintillan D, Darve E and Shaqfeh E S G 2006 Hydrodynamic interactions in the induced-charge electrophoresis of colloidal rod suspensions *J. Fluid Mech.* **563** 223–59
- [49] Rose K, Meier J A, Dougherty G M and Santiago J G 2007 Rotational electrophoresis of striped metallic microrods *Phys. Rev. E* **75** 011503

Supplementary Information

All reference numbers cited in the Supplementary Information (SI) correspond to the references listed at the end of the SI.

A. Linear dependence of the translational and rotational velocity of a nano-object on the boundary conditions in a Stokes flow

Consider an arbitrary rigid object immersed in a Stokes flow, whose hydrodynamic center translates with a velocity \vec{U} while rotating about an axis passing through its geometric center with angular velocity $\vec{\omega}$. The ‘unperturbed’ fluid velocity set up in the device, denoted by $\vec{u}(\vec{r})$ where \vec{r} is the position vector with respect to the hydrodynamic center of the object, will be perturbed by the motion of the object. For a spherical body, this perturbation is negligible beyond 4 object diameters [1, 2, 3]. In the absence of external body forces, the quasi-static Stokes equations for the velocity $\vec{v}(\vec{r})$ and pressure $p(\vec{r})$ are given by [4]

$$\begin{aligned}\nabla p(\vec{r}) &= \mu \nabla^2 \vec{v}(\vec{r}) \\ \nabla \cdot \vec{v}(\vec{r}) &= 0\end{aligned}\tag{1}$$

where μ is the dynamic viscosity of the fluid. Assuming that the fluid does not slip on the surface of the object, the boundary condition for the velocity at a point with position vector \vec{r}_p (with respect to the hydrodynamic center) on the surface of the object is given by

$$\vec{v}(\vec{r}_p) = \vec{U} + \vec{\omega} \times \vec{r}_p\tag{2}$$

Since the flow is assumed to be unbounded, the corresponding boundary condition, at distances far from the object, is that the original flow $\vec{u}(\vec{r})$ is unperturbed by the object,

$$\vec{v}(\vec{r}) \rightarrow \vec{u}(\vec{r}) \quad \text{as } |\vec{r}| \rightarrow \infty\tag{3}$$

This approach gives the force and torque acting on the object (by integrating the shear and pressure distributions on the boundary of the object) in terms of the object geometry and the viscosity, which are known, and the unperturbed flow $\vec{u}(\vec{r})$, which is the flow that we set up using the electrodes in the device. The boundary conditions in Eqns. 2 and 3 can be split into three separate sets of boundary conditions and due to the linear nature of the Stokes flow, the object velocity will be the sum of the velocities due to each of these three sets [4].

The first of the three boundary conditions mentioned above is the ‘stationary’ condition given by

$$\begin{aligned}\vec{v}_{stat}(\vec{r}_p) &= -\vec{u}(\vec{r}_p) \\ \vec{v}_{stat}(|\vec{r}| \rightarrow \infty) &= 0\end{aligned}\tag{4}$$

This corresponds to the case of the object being held stationary in the presence of the unperturbed flow flowing past its surface, which goes to zero at infinity. The second boundary condition is termed the ‘quiescent’ condition, in which the object is moving with the translational velocity \vec{U} and rotating with an angular velocity $\vec{\omega}$ in an otherwise quiescent fluid. The equation for this boundary condition is

$$\begin{aligned}\vec{v}_{qui}(\vec{r}_p) &= \vec{U} + \vec{\omega} \times \vec{r}_p \\ \vec{v}_{qui}(|\vec{r}| \rightarrow \infty) &= 0\end{aligned}\quad (5)$$

The third condition is that of the flow that is unperturbed by the presence of the object.

$$\vec{v}_{unpert}(\vec{r}) = \vec{u}(\vec{r}) \quad \text{for all } \vec{r} \quad (6)$$

The sum of the velocities at the boundary of the object (i.e., at $\vec{r} = \vec{r}_p$), as well as for $|\vec{r}| \rightarrow \infty$, for the three boundary conditions in Eqns. 4, 5, and 6 equals the boundary conditions on the object surface in Eqn. 2 and the boundary condition as $|\vec{r}| \rightarrow \infty$ in Eqn. 3, for the original problem. One can compute the force and torque contributions from each of the three boundary conditions and sum them to get the force and torque for the original set of boundary conditions in Eqns. 2 and 3 [4].

The force and torque on an arbitrary object that comes from the ‘stationary’ boundary condition in Eqn. 4 can be computed by expressing the unperturbed flow $\vec{u}(\vec{r}_p)$ on the surface of the object in terms of a Taylor series expansion about the velocity \vec{u}_o at the center of the object and then integrating the shear and pressure distributions arising from each of the terms in the series [4]. We note here that the same procedure can be carried out for a object having any arbitrary geometry [4].

The force \vec{F}_{qui} and torque \vec{T}_{qui} on an arbitrary object that comes from the ‘quiescent’ boundary condition in Eqn. 5, can always (regardless of object geometry) be expressed in the following form

$$\begin{aligned}\vec{F}_{qui} &= -\mu(\mathbf{K} \cdot \vec{U} + \mathbf{C}^T \cdot \vec{\omega}) \\ \vec{T}_{qui} &= -\mu(\mathbf{C} \cdot \vec{U} + \mathbf{\Omega} \cdot \vec{\omega})\end{aligned}\quad (7)$$

where the matrices \mathbf{K} , \mathbf{C} , and $\mathbf{\Omega}$, whose elements are the drag coefficients, are completely determined by the object geometry (here \mathbf{C}^T is the transpose of \mathbf{C}). We note here that due to the ‘coupling’ matrix \mathbf{C} , one can, for example, have a translational force acting on a object even when it initially starts off from a pure rotational motion (or conversely, a torque from an initial pure translational motion). This type of coupling is exhibited by objects that lack sufficient symmetry, for example, helical screw-shaped objects. However, for orthotropic objects - that is those objects that have three mutually perpendicular planes of symmetry, for example an ellipsoid - the coupling matrix \mathbf{C} is identically zero.

Finally, using Gauss’ divergence theorem, it can be shown that the force and torque on any object from the flow field arising from the ‘unperturbed’ boundary condition (Eqn. 6) is identically zero [6] if the velocity field $\vec{u}(\vec{r})$ is absent of singularities (like sources or sinks) in the interior of the volume occupied by the object.

The resultant force and torque expressions for the stationary and quiescent boundary conditions, when evaluated [4] for an inertia-free ellipsoid in a flow that is a combination of uniform and pure shear flow, yields the translational and rotational velocity expressions stated in the main text.

B. Brownian motion coefficients of an ellipsoidal object

Thermal equilibrium between the fluid and any object suspended in it is maintained by the random collisions between the object and the surrounding fluid molecules. In a given time interval δt these collisions tend to translate and rotate the object along random directions by an amount that is, on average, proportional to $\sqrt{\delta t}$. This proportionality was demonstrated by Einstein [7] and Perrin [8, 9] for translational and rotational Brownian motion for spherical and ellipsoidal objects and is a result of the more general fluctuation-dissipation theorem [10] which can be used to show the inverse relationship between the drag and diffusion coefficients of a spherical object [11]. Brenner extended this result for Brownian motions in all six degrees of freedom of an arbitrarily shaped object [5].

Here, we state Brenner's calculation [5] of the translational and rotational diffusional coefficients of an ellipsoid with principal axes a_1 , a_2 , and a_3 whose surface is given by

$$\frac{x^2}{a_1^2} + \frac{y^2}{a_2^2} + \frac{z^2}{a_3^2} = 1 \quad (8)$$

Define the terms α_β , χ , and $\Delta(\lambda)$ (where λ is a dummy variable) by

$$\begin{aligned} \alpha_i &= \int_0^\infty \frac{d\lambda}{(a_i^2 + \lambda)\Delta(\lambda)} \quad (i = 1, 2, 3) \\ \chi &= \int_0^\infty \frac{d\lambda}{\Delta(\lambda)} \\ \Delta(\lambda) &= [(a_1^2 + \lambda)(a_2^2 + \lambda)(a_3^2 + \lambda)]^{1/2} \end{aligned} \quad (9)$$

The translational diffusion tensor of an ellipsoid \mathbf{D}_T is given by

$$\mathbf{D}_T = \frac{kT}{16\pi\mu} \sum_{i=1}^{i=3} \vec{q}_i \vec{q}_i (\chi + a_i^2 \alpha_i) \quad (10)$$

where k is the Boltzmann coefficient, T and μ are the temperature and dynamic viscosity of the fluid respectively. The term $\vec{q}_i \vec{q}_i$ denotes the tensor formed by the outer product of the unit vector \vec{q}_i with itself (in our situation, $\vec{q}_i \vec{q}_i$ is a 3 X 3 matrix whose $(i, i)^{th}$ entry is 1 and the other eight entries are 0).

The rotational diffusion tensor of an ellipsoid \mathbf{D}_R is given by

$$\mathbf{D}_R = \frac{3kT}{16\pi\mu} (\vec{q}_1 \vec{q}_1 (\frac{a_2^2 \alpha_2 + a_3^2 \alpha_3}{a_2^2 + a_3^2}) + \vec{q}_2 \vec{q}_2 (\frac{a_3^2 \alpha_3 + a_1^2 \alpha_1}{a_3^2 + a_1^2}) + \vec{q}_3 \vec{q}_3 (\frac{a_1^2 \alpha_1 + a_2^2 \alpha_2}{a_1^2 + a_2^2})) \quad (11)$$

where each of the scalars that multiply the three matrices $\vec{q}_i \vec{q}_i$ ($i = 1, 2, 3$), represents the rotational diffusion coefficient about the corresponding axis e_i . The value of the translational diffusion coefficient for a rod in water at 300 K, with $a_1 = 5 \mu\text{m}$ and

$a_2 = a_3 = 100$ nm along the major axis is $0.306 \mu\text{m}^2/\text{s}$ and along the minor axis is $0.199 \mu\text{m}^2/\text{s}$. The rotational diffusion coefficient D_θ , which is the component of \mathbf{D}_R about \hat{z} , is $0.0197 \text{ rad}^2/\text{s}$. The rotational diffusion coefficient is inversely proportional to a_1^3 and is weakly dependent on the aspect ratio $e = \frac{a_2}{a_1}$. In the main text, below Equation 17, we use this functional definition of D_θ , i.e., $D_\theta \equiv \frac{kT}{\mu} \frac{g(e)}{a_1^3}$

B.1 Ratio of rotational to translational diffusion times are completely determined by e for axi-symmetric ellipsoids

Using the transformation $\lambda^* = \frac{\lambda}{a_1^2}$, the shape parameter $e (= \frac{a_2}{a_1})$, and Eqn. 9, for ellipsoids with $a_2 = a_3$ we have

$$\begin{aligned}\alpha_1 &= \frac{1}{a_1^3} \int_0^\infty \frac{d\lambda^*}{(1 + \lambda^*)[(1 + \lambda^*)(e^2 + \lambda^*)^2]^{\frac{1}{2}}} \equiv \frac{1}{a_1^3} \cdot f_{\alpha_1}(e) \\ \alpha_2 &= \frac{1}{a_1^3} \int_0^\infty \frac{d\lambda^*}{(e^2 + \lambda^*)[(1 + \lambda^*)(e^2 + \lambda^*)^2]^{\frac{1}{2}}} \equiv \frac{1}{a_1^3} \cdot f_{\alpha_2}(e) \\ \chi &= \frac{1}{a_1} \int_0^\infty \frac{d\lambda^*}{[(1 + \lambda^*)(e^2 + \lambda^*)^2]^{\frac{1}{2}}} \equiv \frac{1}{a_1} \cdot f_\chi(e)\end{aligned}\quad (12)$$

where $f_{\alpha_1}(e)$, $f_{\alpha_2}(e)$, and $f_\chi(e)$ as defined are each completely determined by e . From Eqn. 10, the translational diffusion coefficient along x and y are given by $D_x = \frac{kT}{16\pi\mu}(\chi + a_1^2\alpha_1)$ and $D_y = \frac{kT}{16\pi\mu}(\chi + a_2^2\alpha_2)$ respectively. Eqn. 11 gives the rotational diffusion component about z as $D_\theta = \frac{3kT}{16\pi\mu}(\frac{a_1^2\alpha_1 + a_2^2\alpha_2}{a_1^2 + a_2^2})$. Thus, using Eqn. 12 we see that the ratio of diffusion times $T_x^\theta(e)$ and $T_y^\theta(e)$ are both, completely determined by e and are given by

$$\begin{aligned}T_x^\theta(e) &= \left(\frac{f_\chi(e) + f_{\alpha_1}(e)}{f_{\alpha_1}(e) + e^2 f_{\alpha_2}(e)} \right) \left(\frac{1 + e^2}{3} \right) \\ T_y^\theta(e) &= \left(\frac{f_\chi(e) + e^2 f_{\alpha_2}(e)}{f_{\alpha_1}(e) + e^2 f_{\alpha_2}(e)} \right) \left(\frac{1 + e^{-2}}{3} \right)\end{aligned}\quad (13)$$

C. Derivation of expression for RMS error for a simple model for orientation control

We describe a simple physical picture of the relation between the RMS error in orientation and the action of the control algorithm at every time step. Our analysis here assumes that there is no time delay in the application of the control, as opposed to the 10 ms delay that was purposely modeled in the simulation. If the control task is to maintain the ellipsoid at an orientation of 0° , we observe from the simulations that the controller spends most of its control authority on maintaining the rod orientation at $\theta = 0^\circ$ (and relatively less authority on position control), thus essentially executing a simple control law: It checks whether the ellipsoid has positive orientation $\theta > 0^\circ$, or negative orientation, $\theta < 0^\circ$, and attempts to apply the maximum allowable shear that can rotate the rod back to $\theta = 0^\circ$. There does exist a maximum allowable shear because the voltage applied at any of the electrodes is not allowed to exceed η_{sat} and one cannot demand that the controller create a flow that rotates the ellipsoid faster

than the shear flow that is dictated by η_{sat} . Within this idealized scenario, the control algorithm is basically an example of *bang-bang* control [12] - a type of control in which the controller abruptly switches between two (or more) states.

The Langevin form [13] of the stochastic differential equation (SDE) for the simple, bang-bang type controller model, that maintains the ellipsoid at $\theta = 0$, is given by

$$d\theta = -\frac{1-e^2}{1+e^2}\sigma_{max} \cdot \text{sign}(\theta)dt + \sqrt{2D_\theta dt} \cdot \mathcal{N}(0, 1) \quad (14)$$

where $e = \frac{a_2}{a_1}$ is the ratio of the minor axis length to the major axis length of the ellipsoid, D_θ is the rotational diffusion coefficient, $\mathcal{N}(0, 1)$ is a random variable with a Gaussian distribution having mean 0 and variance 1, and σ_{max} is the maximum possible shear that can be applied to the particle. Equation 14 means that the controller checks for the sign of the orientation (i.e., whether $\theta > 0$ or $\theta < 0$) and applies the maximum amount of shear σ_{max} in the opposite direction so that the particle returns to $\theta = 0$. With this simplified description of the controller's action, we can write an expression for the RMS error of orientation, which we denote as RMS_{theor} . We first write the following governing equation (the Fokker-Planck equation [13]), for the time evolution of the probability distribution function (pdf) $f(\theta, t)$ of the orientation angle θ at time t , for the SDE 14

$$\frac{\partial}{\partial t}f(\theta, t) = \frac{1-e^2}{1+e^2}\sigma_{max} \cdot \frac{\partial}{\partial \theta}(\text{sign}(\theta)f(\theta, t)) + D_\theta \frac{\partial^2}{\partial \theta^2}f(\theta, t) \quad (15)$$

At steady state, i.e., when the pdf $f(\theta)$ does not change with time, the left hand side of Eqn. 15 equals zero. Integrating the right hand side with respect to θ we get

$$k \cdot \text{sign}(\theta)f(\theta) + \frac{\partial}{\partial \theta}f(\theta) = A \quad (16)$$

where A is some constant and $k = \frac{(1-e^2) \cdot \sigma_{max}}{(1+e^2) \cdot D_\theta}$. When the rod is trapped at $\theta = 0^\circ$, with any reasonable controller, we expect that the nanorod's orientation will be allowed to vary only in a small range of angles around $\theta = 0^\circ$. This implies that the probability that θ is large decreases monotonically and should approach zero for large θ . Hence $f(\theta) \rightarrow 0$ as $\theta \rightarrow \infty$ and $\frac{\partial}{\partial \theta}(f(\theta)) \rightarrow 0$ as $\theta \rightarrow \infty$. Using this in Eqn. 16, we get $A = 0$. Integrating the left hand side of Eqn. 16 with respect to θ , we get

$$f(\theta) \cdot \exp\left(\int_0^\theta k \cdot \text{sign}(\theta)d\theta\right) = B \quad (17)$$

where B is some constant. Thus we get that

$$f(\theta) = B \cdot \exp(-k|\theta|) \quad (18)$$

where $|\theta|$ refers to the absolute value of θ .

By imposing the normalization condition for the pdf $f(\theta)$, i.e. $\int_{-\infty}^{\infty} f(\theta)d\theta = 1$, we get that

$$f(\theta) = \frac{k}{2} \cdot \exp(-k|\theta|) \quad (19)$$

The RMS error (standard deviation) RMS_{theor} of the pdf $f(\theta)$ given in Eqn. 19 is given by

$$RMS_{theor} = \left(\int_{-\infty}^{\infty} \theta^2 \cdot \frac{k}{2} \cdot \exp(-k|\theta|) d\theta \right)^{\frac{1}{2}} \quad (20)$$

Solving the right hand side of the above equation for RMS_{theor} and substituting the value of k gives

$$RMS_{theor} = \sqrt{2} \left(\frac{1 + e^2}{1 - e^2} \right) \left(\frac{D_\theta}{\sigma_{max}} \right) \quad (21)$$

D. Electrophoretic motion of the particle

Suppose that the nanorod is a perfect insulator and the charges inside it cannot be polarized. In such a case the net spatial distribution of the charges in the Debye layer surrounding the nanorod will not change under the applied electric field although the individual ions themselves could move around. For a spatially varying electric field, Sellier[14] considered the case of the electrophoretic motion of a particle with a uniform zeta potential surrounded by a thin Debye layer, that is immersed in an unbounded fluid which is at rest at infinity. So the fluid is not moving due to electro-osmosis as in our device. It only moves due to the perturbation caused by the particle motion. He showed that this motion is linear in the electric field (for translation) and electric field gradient (for rotation). Since the fluid motion is governed by Stokes flow (as stated in Seller's paper and in ours), these particle electrophoretic velocities can be superposed on the particle velocities attained due to electro-osmotic actuation in our device (which are stated in Eqn. 7 of our main paper). This net velocity, both translational and rotational, still show a linear dependence on the electric field and its gradient respectively. However, depending on the sign of the surface charge on the object, its velocity may be reduced by a factor $(1 - \frac{\zeta_p}{\zeta_f})$ due to the mobility being proportional to $(\zeta_f - \zeta_p)$ instead of just ζ_f as stated in the main article (where the particle has its own uniform zeta potential ζ_p while the fluid has a zeta potential ζ_f). Even if $\zeta_p = \zeta_f/2$, the smallest ellipsoid size a_1 that can be controlled (everything else staying the same) should only increase by a factor of $2^{1/3}$ (in accordance with Eqn. 17 of the main text) as compared to the zero electrophoresis case ($\zeta_p = 0$). As a result, this kind of linear electrophoretic motion does not require any changes in our control algorithm.

However one could see nonlinear effects arise due to the polarizability of the object and the associated change in the charge distribution in the Debye layer surrounding the object. This is called induced charge electrophoresis (ICEP) because the electric field induces a charge polarization inside the object which in turn causes the charges in the Debye layer to be polarized. Such a movement of the fluid in Debye layer surrounding the object, will impart an unintended velocity to the object. The translational velocity remains unchanged [15], but the rotational velocity will show a dependence on the square of the electric field strength [15], in a direction that will tend to align the major axis of an ellipsoidal nanorod along the local electric field. In our simulations, the magnitude

of this rotational velocity is negligible due to the low electric field strength as we show below.

For a slender body, the rotational velocity $\vec{\omega}_{ICEP}$ that is (unintentionally) created by our control technique due to induced charge electrophoresis is given by [15]

$$\vec{\omega}_{ICEP} = \frac{\epsilon}{\mu} (\vec{p} \cdot \vec{E}) (\vec{p} \times \vec{E}) \quad (22)$$

where \vec{p} is the unit vector along the major axis of the ellipsoid, \vec{E} is given by

$$\vec{E} = \left(\frac{\vec{p}\vec{p}}{1 + L_{\parallel}} + \frac{\mathbf{I} - \vec{p}\vec{p}}{2(1 + L_{\perp})} \right) \vec{E} \quad (23)$$

where \vec{E} is the unperturbed electric field at the center of the object (by unperturbed, we mean the electric field in the absence of the object). For slender bodies the depolarization factors L_{\parallel} and L_{\perp} associated with the component of the unperturbed electric field along the axes of the ellipsoid, can be approximated by $L_{\parallel} = 0$ and $L_{\perp} = \frac{1}{2}$. In such a case, we can place an upper bound on the magnitude of ω_{ICEP} as

$$|\vec{\omega}_{ICEP}| \leq \frac{\epsilon |\vec{E}|^2}{6\mu} \quad (24)$$

In the simulation in which we rotate the object from an initial orientation of 90° to a final orientation of 0° , we split the simulation into two parts. The first part is the one in which the object orientation is far from the desired value of 0° (this corresponds to the first 1.8 s of the simulation as seen in Fig. 10 of the main paper). The second part of the simulation is when the object is being trapped at 0° . We make this distinction because in the first part, the error in orientation is large and hence the controller is focused on creating a strong shear component of the flow and hence a strong gradient of the electric field. The electric field strength at the center of the object in the first part of the simulation is on average an order of magnitude lower than the second part of the simulation in which the error in orientation is small and hence the controller will have to correct for the position as well as the orientation (correcting for the position means creating a large enough flow velocity, which implies creating a large enough electric field strength).

The mean strength of the electric field at the center of the object in the first part of the simulation is 0.52 V/cm and the mean value of the electric field strength in the second part (while the object is being trapped) is 6.11 V/cm. Using these values of the electric field strengths in Eqn. 24, we get that $\omega_{ICEP} = 3.5 \times 10^{-4}$ rad/s in the first part of the simulation and $\omega_{ICEP} = 4.8 \times 10^{-2}$ rad/s in the second part of the simulation. As noted in the main paper, the rotational velocity applied by our control algorithm using hydrodynamic drag is 0.94 rad/s on average (throughout the simulation). Thus in the first part of the simulation $|\vec{\omega}_{ICEP}|$ is 0.03 % of the rotational velocity applied by our control and at most 5.1 % in the second part of the simulation. In our simulations, we neglect this electrophoretic rotational velocity of the object, i.e., we assume that the movement of the charges in the Debye layer surrounding the object does not affect the object's velocity.

References

- [1] H. Faxen, "The velocity of two spheres that fall under the influence of gravity in a viscous fluid," (Translated title) *Zeitschrift für Angewandte Mathematik und Mechanik*, 7, pp.79-80, 1927.
- [2] M. Stimson and G. B. Jeffrey, "The motion of two spheres in a viscous fluid," *Proceedings of the Royal Society*, A111, pp. 110-116, 1926.
- [3] J. Happel and H. Brenner, *Low Reynolds Number Hydrodynamics*, Englewood Cliffs, Prentice Hall, 1965.
- [4] H. Brenner, "The Stokes resistance of an arbitrary particle - Part IV. Arbitrary fields of flow" *Chemical Engineering Science*, 19, pp. 703-727, 1964.
- [5] H. Brenner, "Coupling between the translational and rotational Brownian motions of rigid particles of arbitrary shape," *Journal of Colloid and Interface Science*, 23, pp. 407-436, 1967.
- [6] H. Brenner, "Effect of finite boundaries on the Stokes resistance of an arbitrary particle" *Journal of Fluid Mechanics*, 12, pp.35-48, 1962.
- [7] A. Einstein, "On the movement of small particles suspended in stationary liquids required by the molecular-kinetic theory of heat," (Translated Title) *Annalen der Physik*, 17, pp. 549-560, 1905.
- [8] F. Perrin, "Brownian Motion of an Ellipsoid (I)," (Translated Title) *Le Journal de Physique et Le Radium*, 7, 5, pp.497-511, 1934.
- [9] F. Perrin, "Brownian Motion of an Ellipsoid (II)," (Translated Title) *Le Journal de Physique et Le Radium*, 7, 7, pp.1-11, 1936.
- [10] H. B. Callen and T.A. Welton, "Irreversibility and Generalized Noise," *Physical Review*, 83, 1, pp.34-40, 1951.
- [11] D. T. Gillespie, "Fluctuation and Dissipation in Brownian Motion," *American Journal of Physics*, 61, 12, pp. 1077-1083, 1993.
- [12] L. Sonneborn and F. Van Vleck, "The Bang-Bang principle for Linear Control Systems," *SIAM Journal On Control*, 2, pp.151-159, 1965.
- [13] N.G. Van Kampen, *Stochastic Processes in Physics and Chemistry* Third Edition, Amsterdam, Netherlands, Elsevier, 2007.
- [14] A. Sellier, "A note on the electrophoresis of a uniformly charged particle," *Quarterly Journal of Mathematics and Applied Mechanics* 55, 4, pp.561-572, 2002.
- [15] D. Saintillan, E. Darve, and E.S.G. Shaqfeh, "Hydrodynamic interactions in the induced-charge electrophoresis of colloidal rod dispersions," *Journal of Fluid Mechanics*, 563, pp.223-259, 2006.